



HAL
open science

Air-Sea fluxes of CO₂ in the Indian Ocean between 1985 and 2018: A synthesis based on Observation-based surface CO₂ , hindcast and atmospheric inversion models

V.V.S.S. Sarma, B. Sridevi, Nicolas Metzl, P. K. Patra, Z. Lachkar, Kunal Chakraborty, C. Goyet, Marina Lévy, M. Mehari, N. Chandra

► **To cite this version:**

V.V.S.S. Sarma, B. Sridevi, Nicolas Metzl, P. K. Patra, Z. Lachkar, et al.. Air-Sea fluxes of CO₂ in the Indian Ocean between 1985 and 2018: A synthesis based on Observation-based surface CO₂ , hindcast and atmospheric inversion models. *Global Biogeochemical Cycles*, 2023, 37 (5), pp.e2023GB007694. 10.1029/2023GB007694 . hal-04084411

HAL Id: hal-04084411

<https://hal.science/hal-04084411>

Submitted on 28 Apr 2023

HAL is a multi-disciplinary open access archive for the deposit and dissemination of scientific research documents, whether they are published or not. The documents may come from teaching and research institutions in France or abroad, or from public or private research centers.

L'archive ouverte pluridisciplinaire **HAL**, est destinée au dépôt et à la diffusion de documents scientifiques de niveau recherche, publiés ou non, émanant des établissements d'enseignement et de recherche français ou étrangers, des laboratoires publics ou privés.

1 **Air-Sea fluxes of CO₂ in the Indian Ocean between 1985 and 2018: A synthesis based on**
2 **Observation-based surface CO₂, hindcast and atmospheric inversion models.**

3

4 VVSS Sarma¹, B. Sridevi¹, N. MetzI², P. K. Patra³, Z. Lachkar⁴, Kunal Chakraborty⁵, C.
5 Goyet^{6,7}, M. Levy², M. Mehari⁴, N. Chandra³

6

7 ¹CSIR-National Institute of Oceanography, Regional Centre, 176 Lawsons Bay Colony,
8 Visakhapatnam, India

9

10 ²LOCEAN/IPSL laboratory, Sorbonne Université, CNRS/IRD/MNHN, Paris, France

11

12 ³Japan Agency for Marine-Earth Science and Technology, Kanagawa, Japan

13

14 ⁴Arabian Center for Climate and Environmental Sciences, New York University Abu Dhabi,
15 Abu Dhabi, United Arab Emirates

16

17 ⁵Indian National Centre for Ocean Information Services, Ministry of Earth Sciences,
18 Hyderabad, India

19

20 ⁶Espace-Dev, UPVD, Perpignan France

21

22 ⁷Espace-Dev, Univ. Montpellier, UPVD, IRD, Montpellier, France

23

24

25 **Abstract**

26

27 The Indian Ocean significantly influences the global carbon cycle but it is one of the
28 undersampled regions in the global ocean with reference to surface ocean pCO₂. As a part of
29 the Regional Carbon Cycle Assessment and Processes-2 (RECCAP2) project, several
30 approaches, such as interpolated observational climatology, hindcast model, observation-
31 based surface CO₂ (empirical models), and atmospheric inversion models have been
32 employed for estimating net sea-to-air CO₂ fluxes between 1985 and 2018. The seasonal,
33 spatial and long-term variability in sea-to-air fluxes of CO₂ were compared with
34 observational climatology. The mean value of CO₂ in the Indian Ocean (north of 37.5°S)
35 using all models is estimated to be -0.19±0.1 PgC yr⁻¹ and it is consistent with the
36 observational climatology (-0.07±0.14 PgC yr⁻¹). The Indian Ocean north of 18°S is found to

37 be the mean annual source ($0.04 \pm 0.05 \text{ PgC yr}^{-1}$) whereas a net sink ($-0.23 \pm 0.11 \text{ PgC yr}^{-1}$) in
38 the south of 18°S . All models captured observed spatial patterns but underestimated the net
39 source of CO_2 in the Oman/Somalia upwelling, the Equatorial Indian Ocean (EIO) and the
40 Bay of Bengal (BoB) whereas CO_2 sink is overestimated in the South Indian Ocean (SIO).
41 Overall, all models captured the seasonality in pCO_2 levels and CO_2 fluxes but overestimated
42 the amplitude of their variability. All models suggested the strengthening of the sink over the
43 period between 1985 and 2018 by $0.02 \text{ PgC yr}^{-1} \text{ decade}^{-1}$. A significant increase in the
44 collection of surface ocean pCO_2 and atmospheric CO_2 measurements improves the model
45 simulations in the Indian Ocean.

46

47 Keywords: Surface pCO_2 ; CO_2 fluxes; Hindcast models; atmospheric inversions; Indian
48 Ocean

49 **1. Introduction**

50

51 The atmospheric carbon dioxide (CO₂) levels are ever increasing since the Industrial
52 Revolution due to several anthropogenic activities such as fossil fuel burning and land-use
53 changes. The enhanced anthropogenic activities led to the acceleration of the rate of CO₂
54 accumulation in the atmosphere from $\sim 1.7 \pm 0.1$ PgC yr⁻¹ in the 1960s to 5.3 ± 0.1 PgC yr⁻¹ in
55 2021 (Friedlingstein et al., 2022). About half of the total anthropogenic emission remains in
56 the atmosphere, and the remaining half is stored in the ocean and land (Canadell et al. 2021).
57 According to the Global Carbon Project assessment of 2022, the ocean has taken up about
58 28% (2.9 ± 0.4 PgC yr⁻¹) of the total anthropogenic CO₂ emissions during 2021
59 (Friedlingstein et al., 2022). It is also well established that the ocean carbon sink increased
60 since the 60s with inter-annual variability (IAV) not fully captured by ocean models.

61

62 The Indian Ocean is a small basin compared to the other two major basins of the Pacific and
63 Atlantic and has a unique geography as it is closed in the north at a low latitude. More than
64 30% of the global population is dwelling along the Indian Ocean coast where rapid
65 industrialization is taking place. As a result, the highest levels of aerosol optical depth (AOD)
66 are observed over the northern Indian Ocean with the highest rate of increase over the globe
67 (Zhang and Reid, 2010; Yadav et al., 2021). The northeastern Indian Ocean (Bay of Bengal;
68 BoB) receives a significant amount of freshwater from major rivers, such as the Ganges,
69 Brahmaputra, and Irrawaddy-Salween systems. The northern Indian Ocean experiences
70 strong seasonality due to a change in direction of monsoonal wind resulting in a reversal in
71 direction of surface currents (Schott and McCreary, 2001), which strongly modulates the
72 biogeochemical cycling of carbon and nitrogen. The northern Indian Ocean is one of the most

73 productive regions in the globe and contributes up to 20% of global ocean primary
74 productivity (Behrenfield and Falkowski, 1997).
75
76 Despite the importance of the Indian Ocean in the global carbon cycle, this region is poorly
77 studied with reference to the biogeochemical cycling of carbon compared to the other two
78 major basins. The seasonal cycle of pCO₂ and carbon fluxes was studied only in the Arabian
79 Sea (George et al., 1994; Goyet et al., 1998; Sarma et al., 1998; 2003; 2013, De Verneil et al.,
80 2022; Chakraborty et al., 2021), the BoB (Sarma et al., 2012; 2015; 2020; 2021; Chakraborty
81 et al., 2021) and the south-western Indian ocean (Metzl et al., 1998) whereas the long-term
82 variability was only recently studied in the southwestern Indian Ocean region (Metzl et al.,
83 2022) as the other regions in the Indian Ocean was either sampled once or twice during last
84 few decades (Takahashi et al., 2009; Sarma et al., 2013). The studies carried out in the aegis
85 of the Joint Global Flux Study (JGOFS) and the Bay of Bengal Process Studies (BoBPS)
86 suggested that the seasonal amplitude of pCO₂ goes beyond 200 µatm in the Arabian Sea
87 (George et al., 1994; Goyet et al., 1998; Sarma et al., 1998; 2003) and BoB (Kumar et al.,
88 1996; Sarma et al., 2012; 2015; 2019). The large amplitude of variability in pCO₂ is driven
89 by variabilities in physical transport, such as upwelling, and convective mixing, in the
90 Arabian Sea, whereas freshwater input by rivers and atmospheric pollutants deposition in the
91 BoB (Sarma et al., 2000; 2012). River discharge displays significant inter-annual variability
92 (Papa et al., 2012). Sarma et al. (2012) found that peninsular rivers bring acidic and high
93 pCO₂ waters to the coast whereas glacial rivers, such as Ganges and Brahmaputra, bring
94 relatively basic and low pCO₂ waters to the BoB. Therefore, the source of river water
95 determines the direction of the flux of CO₂ at the air-sea interface. Kumar et al. (1996)
96 suggested that the BoB is a sink for atmospheric CO₂ in the 1990s whereas Sarma et al.
97 (2015; 2021) found that it is a mild source of the atmosphere due to the deposition of

98 atmospheric pollutants. More recently Sridevi and Sarma (2021) indicated that salinity in the
99 surface waters of the BoB is decreasing over the past two decades due to an increase in the
100 warming of Himalayan glaciers (Goes et al., 2020). Since the pH of the Ganges and
101 Brahmaputra River waters are relatively basic (Sarma et al., 2012), an increase in pH and a
102 decrease in pCO₂ was noticed in the past two decades in the central and eastern BoB (Sridevi
103 and Sarma, 2021).

104

105 Unlike the other two major basins, upwelling is weak in the equatorial Indian Ocean due to
106 the prevalence of westerly winds along the equatorial Indian Ocean (Schott et al., 2009). A
107 flat thermocline is observed in the equatorial Indian Ocean in the east-west direction
108 (Murtugudde and Bualacchi, 1999; Xie et al., 2002). The southern tropical and subtropical
109 region is influenced by the inflow of Pacific waters from the Indonesian Through Flow (ITF)
110 (Schott and McCreary, 2001). A major subduction zone occurs in the South Indian Ocean
111 between 15 and 50°S due to positive wind stress curl (Schott et al., 2009). The subducted
112 water masses are advected to the northern Indian Ocean (Miyama et al., 2003; Schott et al.,
113 2002), carrying nutrients and anthropogenic CO₂ (Sabine et al., 1999). A perennial sink of
114 atmospheric CO₂ was reported in the south Indian Ocean (SIO; Metzl et al., 1991; Poisson et
115 al., 1993; Metzl et al., 1995; 1998; 2022; Metzl, 2009).

116

117 The Indian Ocean experiences strong zonal variability driven by the Indian Ocean
118 Dipole/Zonal Mode (IOD/IODZM) in addition to El Nino-Southern Oscillation (ENSO) and
119 the Southern Annular Mode (SAM) (Saji et al., 1999; Murthugude et al., 2000; Thompson
120 and Solomon, 2002). These climate modes of variability modulate several physical and
121 biogeochemical processes resulting in significant modifications in the CO₂ flux (Sarma 2006;
122 Valsala et al., 2020). The influence of SAM was suggested in the SIO for the period 1991-

123 2007 with large spatial variability in CO₂ growth rate with lower rates in the north of 40°S
124 than south of 40°S during austral winter but higher and uniform rates during austral summer
125 (Metzl, 2009).

126

127 Gruber et al. (2009) identified a significant mismatch between top-down and bottom-up
128 inversion in the tropical Indian Ocean and attributed it to a lack of atmospheric CO₂ data.
129 Sarma et al. (2013) compared CO₂ fluxes from the Indian Ocean between 1990 and 2009
130 using a suite of models (both ocean biogeochemistry and atmospheric inversions) under the
131 aegis of the RECCAP1 project. For the band 30°N-44°S, the median annual sea-air CO₂ flux
132 from models was -0.37 ± 0.06 PgC yr⁻¹ and it was consistent with -0.24 ± 0.12 PgC yr⁻¹ using
133 observations. They further noticed that although all models captured the spatial patterns, CO₂
134 outgassing was underestimated in the upwelling region and overestimated sink in the BoB,
135 whereas CO₂ uptake was underestimated in the subtropical convergence zone.

136

137 Recent use of regional models to study the dynamics of regional ecosystems and
138 biogeochemical cycles in the Indian Ocean revealed an improved representation of key
139 processes relative to global coarse resolution models. For instance, the representation of
140 oxygen minimum zones (OMZ) in the northern Indian Ocean indicates large discrepancies
141 with observations in both CMIP5 and CMIP6 global models, but shows a much-improved
142 agreement with data in regional model simulations, both in terms of their structure, size and
143 intensity (Bopp et al., 2013, Cocco et al., 2013, Kwiatkowski et al., 2020, Al Azhar et al.,
144 2017, Lachkar et al., 2016, 2018, 2021). This was linked to the importance of eddy fluxes -
145 typically inaccurately parameterized in global coarse-resolution models but resolved in finer-
146 resolution regional models – in shaping OMZs (e.g., Lachkar et al., 2016, Bettencourt et al.,
147 2015, Brandt et al., 2015, Chakraborty et al., 2019). Furthermore, accurately representing the

148 structure and intensity of these low-O₂ bodies in regional models is critical to represent their
149 recent and future changes under ongoing climate change (Lachkar et al., 2021). Mesoscale
150 eddies were also shown to have a significant impact on the carbon cycle in the northern
151 Indian Ocean (Sarma et al., 2016; 2019; 2021). Additionally, significant improvements in
152 parameterizations of river discharge, monsoon mixing and associated biological response in
153 the high-resolution regional models lead to a better representation of the upper ocean cycle in
154 the regional models (Chakraborty et al., 2018; 2021; Ghosh et al., 2022; Valsala et al., 2021).
155 Therefore, eddy-resolving regional models may lead to an improved representation of the
156 carbon cycle in the region. This work aims to evaluate the net air-sea CO₂ fluxes by different
157 global and regional models and quantify how these simulated net CO₂ fluxes in the Indian
158 Ocean are comparable with observational climatology and identify potential reasons for
159 deviations, if any, in the Indian Ocean.

160

161 **2. Methods**

162

163 2.1. Study region

164

165 Based on the RECCAP2 regional definitions, the entire Indian Ocean, north of 37.5°S, was
166 considered as one region. Due to the complexity of the regional physical processes in the
167 Indian Ocean, we define here the following five regions for analysis: i) the entire Indian
168 Ocean (30°N-37.5°S), ii) the Arabian Sea (0-30°N; 38-78°E), iii) the Bay of Bengal (BoB; 0-
169 30°N; 78-110°E), iv) Equatorial Indian Ocean (EIO; 0-18°S) and v) South Indian Ocean (SIO;
170 18°S-37.5°S) (Figure 1a).

171

172 2.2 Data sets

173

174 To describe the regional CO₂ fluxes for the Indian Ocean, RECCAP2 global CO₂ flux
175 products were used that include observations (climatology referenced to the year 2000;
176 Takahashi et al., 2009), Global hindcast (GHM), regional hindcast (RHM) models,
177 observation-based (empirical) surface pCO₂ models and atmospheric inversion models.

178

179 2.2.1. Observational climatology

180

181 The Indian Ocean is one of the least sampled basins in the world ocean for surface pCO₂
182 measurements with reference to space and time (Figure 1b; Bakker et al., 2016). The major
183 addition of data was done during 1990-1999 whereas in the next decade (2000-2009) some
184 data were added in the SIO and one transect in the BoB and good coverage of the Bay was
185 done in 2010-2019 (Bakker et al., 2020; Supplementary Figure S1). Within the Indian Ocean,
186 the seasonal and inter-annual pCO₂ data are available in the western basin (the Arabian Sea
187 and the southwestern Indian Ocean). In contrast, only 2 to 3 times were sampled in the
188 eastern basin (Supplementary Figure S1). In addition to this, time-series pCO₂ (water and air)
189 data are available in the central BoB, as a part of the RAMA (Moored array for African-
190 Asian-Australian Monsoon Analysis and Prediction) buoy program (BOBOA, Sutton et al,
191 2019), from 2013 onwards (Figure 1). Nevertheless, understanding seasonality in pCO₂ is a
192 challenge in the Indian Ocean due to the weak spatial and seasonal data coverage. Takahashi
193 et al. (2009) (Figure 1c) compiled the available pCO₂ data in the Indian Ocean and gridded it
194 to 4° x 5° using two-dimensional advection-diffusion equations to interpolate with reference
195 to space and time. The major challenge here is that the observations (henceforth called
196 climatology) are not absolutely observations alone but were interpolated in the regions where
197 data were unavailable. There is uncertainty associated with the techniques used for

198 developing climatology. Due to the lack of seasonal data in some regions, the seasonality
199 shown in the data is significantly driven by the model used to interpolate. However, the
200 performance of the seasonality driven by the model used to derive climatology is tested using
201 pCO₂ data generated by the BOBOA buoy in the central BoB. Nevertheless, the observed
202 CO₂ fluxes carry several errors due to sparse coverage of data, wind speed measurements and
203 transfer velocity parameterizations and the uncertainty of the CO₂ fluxes is about 50%
204 (Gruber et al., 2009).

205

206 Since RECCAP1 (Sarma et al., 2013) important progress has been made on both pCO₂ data
207 delivery each year in the public domain for updating SOCAT data-product (www.socat.info,
208 Pfeil et al., 2013; Bakker et al., 2014, 2016) and the development of empirical methods that
209 reconstruct pCO₂ fields, including in synthesis studies (SOCOM project, Rödenbeck et al.,
210 2015). Here we used 9 empirical methods based on the SOCAT data (version v2020) and to
211 compare our new results with RECCAP1, we also used the original climatology of Takahashi
212 et al (2009) (Figure 1c). Recall that climatology was constructed for the reference year 2000
213 which would have to be taken into account when comparing pCO₂ fields for the recent year.
214 However, this would not dramatically impact the mean CO₂ fluxes assuming that over 1985-
215 2018 ocean pCO₂ increase is close to the atmospheric growth rate as observed in some parts
216 of the Indian Ocean (e.g. Metzl, 2009; Lauvset et al., 2015; Metzl et al., 2022; Lo Monaco et
217 al., 2021).

218

219 2.2.2. Ocean Hindcast models

220

221 CO₂ fluxes and surface water pCO₂ data were obtained from 12 GHM and 2 RHM (Table 1).

222 These models represent physical, chemical and biological processes controlling the marine

223 carbon cycling and exchange of CO₂ at the sea-to-atmosphere interface. The GHM have a
224 coarse or an eddy-permitting horizontal resolution whereas RHM is eddy-resolving (Table 1).
225 The simulations are forced with meteorological reanalysis products, given in Table 1. The
226 models were run for different periods mostly between 1980 and 2019 with the period of each
227 model given in Table 1. In order to make it uniform for all models, we have considered the
228 runs between 1985 and 2018 in this study that gives the reference year of 2002. GHM and
229 RHM have been integrated from the pre-industrial period to the present day with the same
230 atmospheric CO₂ history. Although the model simulations were carried out following the
231 RECCAP2 ocean modelling protocol, each model is different from others with respect to
232 forcing, experimental configuration, representation of biogeochemical processes and sub-grid
233 parameterizations (Table 1).

234

235 2.2.4. Atmospheric inversions

236

237 Atmospheric inversions (top-down) estimate the surface CO₂ fluxes based on the variability
238 in the measured atmospheric CO₂ using an atmospheric transport model. In the atmospheric
239 inversion models, a priori information about the surface CO₂ fluxes is used from bottom-up
240 estimates (e.g., Takahashi et al., 2009) or an ocean GHM or an empirical upscaling model. In
241 the Indian Ocean region and surrounding, atmospheric CO₂ measurements are available from
242 only 8 sites that are used in the atmospheric inversion models. Among them, only two
243 stations have long-record and others have short records. However, most inversions did not
244 correct the oceanic prior fluxes significantly when the empirical upscaling model fluxes were
245 used. Here we have chosen to show sea-air CO₂ fluxes from inversion models, one using
246 prior flux from Takahashi et al. (2009) in the MIROC4-ACTM system (Chandra et al., 2022)
247 and the other model (CAMsv20r1) using prior fluxes from an empirical model (Chevallier et

248 al., 2005). The atmospheric inversion model runs are available between 2001 and 2018 which
249 gives the reference year of 2009.

250

251 2.2.5. Observation-based Surface pCO₂ (Empirical models)

252

253 Global sea-air CO₂ fluxes can also be estimated from pCO₂ measurements along the ship
254 tracks over the past several decades. The first and simple upscaling method was implemented
255 by Takahashi et al. (2009) where all the past measurements of CO₂ are separated in monthly-
256 mean flux maps based on SST and salinity. This method relied on the extrapolation of
257 Delta_pCO₂ data from limited measurements along the cruise tracks to the global ocean. With
258 the development of neural networks and other artificial intelligence tools and organised
259 archival of the SOCAT CO₂ database, several methods are now implemented to calculate
260 gridded CO₂ flux including the interannual variation, taking into account the physical state of
261 sea-surface conditions (Table 2; Rödenbeck et al., 2015; Landschützer et al., 2016; Fay et al.,
262 2021). The estimated CO₂ fluxes between 1985 and 2018 were considered in this study with
263 the reference year of 2002.

264

265 **3. Results and Discussion**

266

267 The simulations of CO₂ uptake by the Indian Ocean by GHM, RHM, empirical and
268 atmospheric inversion models are compared with climatology with reference to (i) annual, (ii)
269 seasonal and (iii) interannual timescales.

270

271 3.1. Annual mean CO₂ fluxes in the Indian Ocean between 1985 and 2018

272

273 3.1.1. Tropical Indian Ocean (north of the 37.5°S)

274

275 The annual mean sea-air CO₂ fluxes for 1985 to 2018 are presented in Table 3 and Figure 1d
276 for the entire Indian Ocean (37.5°S –30°N; 25-125°E), Arabian Sea (30-78°E and 0-30°N),
277 BoB (78-110°E and 0-30°N), EIO (30-125°E, 0-17°S) and SIO (37.5-17°S and 25-130°E).

278 The spatial variability in mean annual uptake for the entire Indian Ocean by GHM and RHM
279 (Figure 2), empirical (Figure 3) and atmospheric models (Figure 4) are given to evaluate the
280 spatial variability in CO₂ fluxes.

281

282 The simulated mean annual CO₂ sea–air fluxes by different models varied between -0.27 and
283 -0.13 PgC yr⁻¹ for the Indian Ocean (Table 3), with a relatively lower sink estimated by
284 empirical models (-0.13±0.04 PgC yr⁻¹) than hindcast (-0.21±0.10 PgC yr⁻¹) and
285 atmospheric inversion models (-0.27±0.16 PgC yr⁻¹). Both hindcast and atmospheric
286 inversion models overestimated the sink of CO₂ by 3 times that of climatology (-0.07±0.14
287 PgC yr⁻¹) whereas empirical models are close to the observations. The observational pattern
288 of CO₂ flux shows that the SIO is a dominant sink whereas the Arabian Sea is a strong source
289 while EIO and the BoB are weak sources of atmospheric CO₂. All models simulated similar
290 patterns of spatial variations of the CO₂ fluxes (Figures 2 to 4) that are in agreement with
291 observations, but the magnitudes of fluxes are different. For instance, the modelled CO₂
292 fluxes were spread around the climatological values with relative overestimation of the sink
293 in the south of 22°S, in contrast, underestimation of the source was noticed by all models in
294 the north of 22°S in the Indian Ocean. In contrast, the RHM (both INCOIS-BIO-ROMS and
295 ROMS_NYUAD) reproduced CO₂ fluxes well in comparison with the climatology. Since the
296 ROMS_NYUAD model simulation was submitted up to 31.5°S only, we did not include it in
297 the SIO region as it was considered up to 37.5°S for other models. Similarly, the simulated

298 CO₂ fluxes by empirical models are in good agreement with the climatology (Figure 3). In the
299 case of the atmospheric inversions, a higher CO₂ sink in the south of 15°S whereas sources of
300 CO₂ in the north of 15°S than the observational climatology was observed (Figure 4). The
301 CO₂ fluxes by all models are in near perfect agreement with each other for the entire Indian
302 Ocean within the standard deviation of the estimates, however, they are different on the
303 regional subdivisions such as the Arabian Sea, BoB, EIO and SIO.

304

305 The standard deviation for the atmospheric inversion was large in the annual uptake (-
306 0.27 ± 0.16 PgC yr⁻¹) while the smallest for the empirical models (-0.13 ± 0.04 PgC yr⁻¹; Table
307 3). The highest standard deviation in the atmospheric inversion comes from the sparse
308 atmospheric CO₂ measurements, transport model uncertainties and differences in the prior
309 flux assumptions for the Indian Ocean. The atmospheric CO₂ time series data are available
310 only at 8 locations within the Indian Ocean resulting in high variability in the estimates. The
311 climatology also has a very high standard deviation (-0.07 ± 0.14 PgC yr⁻¹) due to a lack of
312 enough data in the Indian Ocean as most of the Indian Ocean region is either sampled once or
313 twice and inter and extrapolation of the data (Takahashi et al., 2009).

314

315 The zonal integrated CO₂ fluxes by different models are given in Figure 5 and it shows that
316 most of the GHM underestimated CO₂ sink in the south of 25°S whereas over estimated north
317 of 25°S. The RHM (INCOIS-BIO-ROMS and ROMS_NYUAD) simulated exceptionally
318 well the zonal mean CO₂ fluxes in the Indian Ocean between 37.5°S and 27.5°N. However, a
319 slight underestimation was noticed for both the RHM and GHM in the north of 5°N (Figure
320 5a). In the case of empirical models (Figure 5b), Jena-MLS, JMAMLR and UOEX_WAT20
321 were over-estimated in the south of 15°S and well performed in the north of 15°S with
322 reference to climatology. In the case of atmospheric inversions, a stronger sink is noticed in

323 the south of 15°S and a stronger source in the north of 10°S, compared to the empirical and
324 hindcast models (Figure 5c).

325

326 Both spatial variations and zonal integration in the CO₂ fluxes (Figures 2-5) suggest that the
327 model simulations significantly deviated from the climatology at several zones, namely the
328 Oman/Somali upwelling region in the Arabian Sea, freshwater discharge region in the BoB,
329 equatorial upwelling region and south equatorial current (SEC) and subtropical convergence
330 zone regions in the southern tropical Indian Ocean. The potential reasons responsible for the
331 regional variations in the CO₂ fluxes were discussed in detail below.

332

333 **3.1.2. Northwestern Indian Ocean (Arabian Sea)**

334

335 The Arabian Sea is simulated as a net source of CO₂ to the atmosphere by the hindcast
336 models (0.006 to 0.058 PgC yr⁻¹ with a mean of 0.03±0.01 PgC yr⁻¹), empirical models
337 (0.052 to 0.098 with a mean of 0.08±0.01 PgC yr⁻¹) and atmospheric inversions (0.16±0.12
338 PgC yr⁻¹; Table 3) and it is consistent with the observations (Sarma, 2003; Goyet et al., 1998;
339 Millero et al., 1998) and climatological fluxes (0.08±0.06 PgC yr⁻¹) (Table 3). Considering
340 the standard deviation of climatology, and models, the mean of all modelled fluxes in the
341 Arabian Sea (0.06±0.05 PgC yr⁻¹) is close to that of climatology (0.08±0.06 PgC yr⁻¹; Table
342 3). The large source of CO₂ to the atmosphere from the Indian Ocean is driven by the
343 upwelling off Oman/Somali coasts, where pCO₂ levels as high as >600 µatm were reported
344 during the peak southwest monsoon period (Körtzinger et al., 1997; Goyet et al., 1998; Sarma,
345 2003; Sabine et al., 2000). Most of the models poorly simulated CO₂ fluxes in the
346 Oman/Somali upwelling region (Figures 2-4). Within the hindcast models, both MRI-ESM2-
347 1 and ROMS_NYUAD models simulated CO₂ fluxes close to the observations (Figure 2).

348

349 The simulation of upwelling in the Arabian Sea may be a challenge due to the complex
350 interplay of winds, bottom topography, monsoonal circulation and mixing, to capture the
351 observed response by the models. The monsoon mixing is intense during summer (June to
352 September) resulting in high pCO₂ levels in the entire Arabian Sea with maximum off Oman
353 and Somalia coasts (Sarma et al., 1996; 1998; Goyet et al., 1998; Körtzinger et al., 1997). It
354 was estimated that the mixing effect is a dominant controlling factor of surface ocean pCO₂
355 in the Arabian Sea during the monsoon period while biological effect, mainly bacterial
356 degradation, dominates during the non-monsoon period (Louanchi et al., 1996; Sarma et al.,
357 2000). All hindcast models failed to simulate the monsoon mixing well resulting in weaker
358 fluxes of CO₂ (Figure 2) to the atmosphere. Since empirical models are mainly driven by
359 observations, they could simulate the impact of upwelling on pCO₂ reasonably well (Fig. 3).
360 In the case of atmospheric models, MACTM over-estimated coastal upwelling whereas
361 CAMSv20r1 remained close to that of the prior flux field from CEMES_LSCE_FFNN
362 (Figure 4). Sarma et al. (2013) noticed weak mixing in the GHM, and ocean inversion models
363 in the Arabian Sea between 1990 and 2009 and no improvements were noticed with reference
364 to mixing in the Arabian Sea in the past decade.

365

366 To examine the variability in the simulation of mixing in the Oman/Somalia upwelling
367 regions by different GHM and RHM, the sea surface temperature (SST) simulated by the
368 hindcast models was compared (Supplementary Figure S2). All models simulated upwelling
369 features off Oman/Somalia region, however, the intensity of mixing was different among
370 models, as reflected in the SST. It was noticed that mixing was weaker in CCSM-WHOI, EC-
371 Earth3, MOM6-Princeton, NorESM-OC1.2, ORCA025-GEOMAR and Planktom12 models
372 than in other GHM as former models showed relatively warmer SSTs than later models

373 compared to the climatology. Since a significant amount of data was contributed to the
374 climatology from the Oman/Somali upwelling region, we can confidently attribute that the
375 mixing and pCO₂ input from the subsurface layers in the Oman/Somalia upwelling region
376 needs to be improved in the GHM for accurate simulations.

377

378 3.1.3. Northeastern Indian Ocean (Bay of Bengal)

379

380 All models simulated that the BoB is a mild source of CO₂ (0.00 to 0.01 PgC yr⁻¹ with a
381 mean of 0.00±0.01 PgC yr⁻¹) and it is consistent with the climatology (0.01±0.01 PgC yr⁻¹;
382 Takahashi et al., 2009; Table 3). Sarma et al. (2012) reported that the peninsular river
383 discharge increased the pCO₂ levels whereas glacial rivers (Ganges and Brahmaputra)
384 discharge decrease the pCO₂ levels (Kumar et al., 1996; Mukhopadhyay et al., 2002). More
385 recently Sarma et al. (2019) reported that cyclonic eddies enhance pCO₂ levels due to
386 upwelling in the core of the eddy while anticyclonic eddies sink for atmospheric CO₂. Several
387 recent investigations suggested that rapid acidification is being occurred in the BoB due to
388 the deposition of atmospheric pollutants (Sarma et al., 2015; 2021; Kumari et al., 2022a,b)
389 leading to an increase in pCO₂ levels. Unfortunately, neither GHM nor RHM has the
390 atmospheric component to consider its impact.

391

392 Since river discharge enhances the CO₂ sink to the BoB, the differences in the sink of CO₂ in
393 the BoB may be caused by variable use of river discharge data as this would influence the
394 salinity of the upper ocean in the BoB. The existence of a strong linear relationship between
395 salinity and pCO₂ levels was reported in the BoB (Kumar et al., 1996; Sarma et al., 2012;
396 2021). Recently, Sridevi and Sarma (2021) observed decreasing trends in surface pCO₂ levels
397 due to a decrease in salinity over the past two decades due to the warming of Himalayan

398 glaciers (Goes et al., 2020). Therefore, salinity is a crucial parameter in controlling the pCO₂
399 levels in the BoB.

400

401 To examine this, the salinity simulations by different models were examined (Supplementary
402 Figure S3). All GHM simulated low salinity in the northern Bay but the magnitude of salinity
403 is different in the north of 15°N. The lower salinity in the northern Bay was simulated in
404 CCSM-WHOI, MOM6-Princeton and ORCA1-LIM3-PISCES, whereas relatively high
405 salinity was simulated in CNRM-ESM2-1 and Planktom12. However, the sink in CO₂ was
406 observed in both high and low-salinity simulated models suggesting that variability in the
407 sink of CO₂ is not caused by river discharge/salinity in the GHM. An insignificant
408 relationship was observed between salinity and pCO₂ levels among different GHM and RHM
409 in the northern BoB (Figure is not shown) suggesting salinity or river discharge may not be a
410 controlling factor on variable CO₂ fluxes in the BoB. The absence of a relationship between
411 salinity and pCO₂ levels in the models suggests that the role of freshening surface waters by
412 rivers was not well constrained in the hindcast models.

413

414 3.1.4. Equatorial Indian Ocean (EIO)

415

416 The empirical models (0.02 ± 0.02 PgC yr⁻¹) and atmospheric inversions models (0.02 ± 0.03
417 PgC yr⁻¹) simulated a mild source of the atmospheric CO₂ and it is consistent with the
418 climatology (0.04 ± 0.03 PgC yr⁻¹), in contrast, hindcast models estimated sink (-0.05 ± 0.04
419 PgC yr⁻¹) in the EIO. All models simulated that the western equatorial Indian Ocean is a
420 source whereas the eastern region is either a sink or close to balance. The higher sink
421 simulated by GHM is caused by weaker Somalia upwelling as discussed in section 3.1.2.
422 RHM simulated that the equatorial Indian Ocean is a mild source of atmospheric CO₂

423 (0.01±0.06 and 0.03±0.08 PgC yr⁻¹ by ROMS-NYUAD and INCOIS-BIO-ROMS
424 respectively). This can be noticed from the spatial distribution of SST, which is relatively
425 warmer in the GHM in the western equatorial region compared to the RHM (Supplementary
426 Figure S4) suggesting better simulation of upwelling in the RHMs. The spatial variations in
427 CO₂ fluxes by RHM and atmospheric inversions (Figures 2 and 4) are consistent with the
428 observations in the EIO region (Figure 1c).

429

430 3.1.5. The South Indian Ocean (SIO)

431

432 The SIO comprises two key oceanographic regimes of oligotrophic waters in the north and
433 Southern Ocean waters in the south. These two regions are separated by the subtropical front
434 (STF). We have considered the STF region as part of the SIO in this study. The estimated
435 mean fluxes in this region by all models are -0.23±0.11 PgC yr⁻¹ suggesting a strong sink of
436 atmospheric CO₂ that agrees well with climatology (-0.20±0.16 PgC yr⁻¹; Table 3). The
437 atmospheric inversions estimated a larger sink (-0.46±0.3 PgC yr⁻¹), which is mainly caused
438 by MATCM whereas the CAMSv20r1 model performed well by staying close to the prior
439 model. Despite atmospheric observations available in the SIO at Amsterdam Island at 38°S,
440 the overestimation of the sink by the atmospheric model must be examined. Both empirical
441 models (-0.22±0.04 PgC yr⁻¹) and hindcast models, including RHM, (-0.20±0.07 PgC yr⁻¹)
442 estimated CO₂ fluxes close to that of climatology (-0.22±0.04 PgC yr⁻¹). The CO₂ fluxes in
443 the SIO are closer in magnitude to the annual uptake for the entire Indian Ocean (-0.19±0.1
444 PgC yr⁻¹) indicating that the majority of the net uptake of CO₂ occurs in the SIO, as suggested
445 by other studies (Sabine et al., 2000; Bates et al., 2006; Metzl, 2009; Takahashi et al., 2009;
446 Sarma et al., 2013).

447

448 The spatial variability in the magnitude of CO₂ flux within the SIO was variable among
449 hindcast models (Figure 2) in comparison to climatology (Figure 1c). For instance, the
450 climatology suggests a strong sink between 15°S and 35°S whereas the sink was simulated by
451 most of the hindcast models between 10°S and 25°S. Sabine et al. (1999) observed the highest
452 concentration and deepest penetration of anthropogenic carbon in the subtropical
453 convergence zone (30-40°S). In contrast, a mild source is simulated by most of the models in
454 the south of 30°S suggesting that the sink was underestimated in this zone. The outcropping
455 of these density surfaces and the subsequent sinking of surface waters provide a pathway for
456 excess CO₂ to enter the interior of the ocean. Overestimation of the CO₂ uptake by the
457 models in these zones suggests that vertical mixing was not constrained properly in the
458 models, leading to excess deep mixing, which increased surface water pCO₂ and a decrease in
459 the flux of the ocean (Figure 2).

460

461 3.2. Seasonal variations in pCO₂ levels and air-sea CO₂ fluxes in the Indian Ocean

462

463 To examine the seasonal variability of CO₂ fluxes by various modelling approaches, the
464 simulated surface pCO₂ levels and CO₂ fluxes were analysed (Figure 6). This provides
465 insights into the ability of the models to represent the complex interplay of physical and
466 biological processes on pCO₂ levels and sea-air CO₂ exchange. The ability of a model to
467 reproduce the seasonal cycle also provides some reassurance that the models are correctly
468 projecting climate sensitivity of the processes that could influence long-term projections of
469 the ocean CO₂ uptake (Fig. 6).

470

471 3.2.1. The Entire Indian Ocean

472

473 The increase in pCO₂ levels is expected in the tropical Indian Ocean between June and
474 September due to an increase in mixing driven by the southwest monsoon in the north
475 whereas deeper mixing in the SIO (Louanchi et al., 1996; Sarma et al., 2000; Sabine et al.,
476 2000; Bates et al., 2006). All hindcast models overestimated the sink between June and
477 September but were close to observation during other months (Fig. 6) due to weak mixing of
478 pCO₂-rich subsurface waters with surface. Among the other models, ROMS-NYUAD and
479 MPIOM-HAMOCC displayed relatively better seasonality in CO₂ fluxes compared to
480 climatology (Figure S5). The mean empirical models followed seasonality close to that of
481 observations. The atmospheric inversions overestimated the sink from March to October
482 mainly in the SIO compared to other models and climatology. Since the seasonality in CO₂
483 fluxes is variable with space, the same in different regions of the Indian Ocean are examined.

484

485 3.2.2. Northwestern Indian Ocean (Arabian Sea)

486

487 The Arabian Sea shows strong seasonality with higher CO₂ fluxes from June to September
488 associated with monsoon mixing and high winds compared to other seasons (George et al.,
489 1994; Sarma et al., 1996; 1998; Sarma, 2003). The climatological amplitude of seasonality
490 was close to 0.2 PgC yr⁻¹ with a maximum in June-August and a minimum in October-
491 December (Figure 6). The seasonality was perfectly captured by the empirical models
492 whereas atmospheric inversion and hindcast models failed to simulate as they over and
493 underestimated respectively. Though atmospheric inversion models mostly captured the high
494 CO₂ fluxes to the atmosphere from June to August but with a large spread compared to other
495 simulations by hindcast and empirical models. In contrast, hindcast models showed a
496 response but it was strongly out of phase with the observations by giving maximum fluxes in
497 May to June and minimum fluxes in July to September with approximately 3-4 months ahead

498 of the climatological peak in CO₂ fluxes. The two GHM (MRI-ESM2-1 and NorESM-OC1.2)
499 and RHM (ROMS-NYUAD) simulated peak fluxes between June and August in the Arabian
500 Sea (Figure S5).

501

502 All GHM failed to simulate seasonality in pCO₂ (Figure 6) levels as the higher pCO₂ levels
503 were observed during July to September in the observations whereas April to May in the
504 models. High pCO₂ levels were reported from June to August due to enhanced vertical
505 mixing caused by monsoon winds in the Arabian Sea (Sarma et al., 1996; 1998; Körtzinger et
506 al., 1997; Millero et al., 1998; Sarma, 2003). Sarma et al. (2000) observed that mixing is the
507 dominant controlling factor of pCO₂ levels from June to August in the Arabian Sea followed
508 by biological effects (Louanchi et al., 1996; Goyet et al., 1998). The difference in pCO₂
509 levels between mean hindcast models and observations varied between 15 and 50 µatm
510 whereas it was <20 µatm in the case of empirical models (Figure 6). The reference year for
511 climatology is 2000 (Takahashi et al., 2009) whereas the reference year for hindcast and
512 empirical models are 2002 (1985-2018). The difference in pCO₂ levels caused by variable
513 reference year may differ up to 4 µatm considering the 2 µatm/y as a growth rate of surface
514 ocean pCO₂ (Metzl, 2009) suggesting that weaker mixing in the models underestimated the
515 seasonality in pCO₂ and CO₂ fluxes in the Indian Ocean.

516

517 3.2.3. Northeastern Indian Ocean (Bay of Bengal; BoB)

518

519 The BoB also displayed large seasonality with higher CO₂ fluxes from May to August
520 associated with monsoon mixing and decreased between October and December due to river
521 discharge and stratification (Figure 6; Sarma et al., 2016; 2018; 2019). All models simulated
522 high CO₂ fluxes during May but decreased to low by July-August (Figure 6). The observed

523 amplitude of seasonality was close to 0.02 PgC yr^{-1} with the maximum in May-June (0.02
524 PgC yr^{-1}) and minimum in February (0 PgC yr^{-1}). The mean hindcast models simulated
525 similar amplitude (0.02 PgC yr^{-1}) but they showed sink (0 and $-0.02 \text{ PgC yr}^{-1}$) instead of
526 source in the climatology. The atmospheric inversion models displayed too low (high sink
527 during February) and high source from August to October.

528

529 All GHM simulate seasonality in pCO_2 levels in the BoB with a maximum in April and May
530 and a minimum in February (Figure 6). The magnitude of seasonal variability in pCO_2 is ~ 15
531 μatm in the climatology whereas hindcast models simulated $15\text{-}40 \mu\text{atm}$ with lower
532 variability ($<20 \mu\text{atm}$) during April and May and higher ($>35 \mu\text{atm}$) during other months. The
533 underestimation of pCO_2 in the BoB may be caused by strong stratification in the model
534 leading to lower input from pCO_2 -rich subsurface waters. In addition to this, the difference
535 between simulations and observation may also be caused by the lack of enough data in the
536 observations as the BoB is severely under-sampled with reference to seasons. To resolve this
537 issue, the pCO_2 data collected by the BOBOA mooring buoy in the central BoB (Figure 1a) is
538 used for comparison. This buoy collected data between 2013 and 2018 (Sutton et al 2019)
539 and the monthly climatology of this data was compared with Takahashi climatology. The
540 BOBOA climatology showed an increase in pCO_2 starting in April with a peak in May
541 whereas Takahashi climatology displayed during April suggesting that Takahashi
542 climatology well reproduced the observed seasonality although the climatology was not
543 constrained with BOBOA data. Most of the hindcast models displayed peaks in April-May in
544 the BoB and were also consistent with the climatology (Figure S5).

545

546 3.2.4. Equatorial Indian Ocean (EIO)

547

548 The CO₂ fluxes in the EIO displayed seasonality with high fluxes from January to May and
549 low from June to October with a minimum in August (Figure 6). The mean observed CO₂
550 fluxes are the source of the atmosphere during all seasons whereas all hindcast models
551 simulated sink, especially between May and November. All models displayed similar
552 seasonal variability in CO₂ fluxes but underestimated from May to November. The RHM
553 simulated better seasonality in the CO₂ fluxes compared to GHM (Figure S5).

554

555 The EIO displays relatively weak pCO₂ seasonality with a high from February to April and a
556 low from June to October. The amplitude of seasonality in pCO₂ was <10 µatm in the
557 climatology. All models simulated the seasonality but they were under-estimated pCO₂ by
558 ~20 µatm from that of climatology (Figure 6).

559

560 3.2.5. The South Indian Ocean (SIO)

561

562 The SIO displayed large seasonality in fluxes with CO₂ source during January to March and
563 CO₂ sinks during other months (Figure 6). All models reproduced seasonality very well in
564 the SIO (Figure S5).

565

566 All GHM simulate seasonality in pCO₂ levels in the SIO with a maximum in January and
567 March and a minimum in July-August. The magnitude of seasonal variability in pCO₂ is ~15
568 µatm in the climatology whereas hindcast models simulated <20 µatm. The difference in
569 pCO₂ between simulation and observations was up to 40 µatm (Figure S5). The large
570 difference in pCO₂ seasonality in the SIO may be caused by weaker mixing simulations in the
571 models in austral winter and the opposite in summer.

572

573 3.3. Interannual variability (IAV)

574

575 The interannual variability and trends in pCO₂ levels and their fluxes at the air-water
576 interface was also investigated in 1985-2018 using different models (Figure 7). The rate of
577 increase in surface ocean pCO₂ levels varied from 1.54 to 1.73 μatm yr⁻¹ between 1985 and
578 2018 with a lower rate of increase in the BoB and higher in the EIO and SIO. The growth rate
579 of pCO₂ in the surface waters by both hindcast and empirical models is close to that of
580 atmospheric growth and observed surface pCO₂ growth in the Southwestern Indian Ocean
581 (Metzl, 2009; Lo Monaco et al., 2021; Leseurre et al., 2022). Due to the lack of basin-scale
582 observational time-series data in the Indian Ocean, the performance of the IAV by the models
583 cannot be assessed. Given the variability of IOD and ENSO index (Figure 7), we divided the
584 IAV trends into three timelines, i.e., a) 1985-2000, b) 2001-2018 and c) 1985 to 2018 (Figure
585 7; Tables 4 and 5) to examine the possible changes in growth rate in the recent decades from
586 that of earlier. To avoid biasing the magnitude of the seasonality, we first de-trend the
587 simulated time series of IAV.

588

589 3.3.1. The entire Indian Ocean

590

591 Both hindcast and empirical models simulated IAV in the surface pCO₂ levels in the entire
592 Indian Ocean as 1.67 to 1.70 μatm yr⁻¹ between 1985 and 2018. The rate of increase in pCO₂
593 levels was lower from 1985 to 2000 (1.41-1.49 μatm yr⁻¹) and increased in the recent decades
594 (2001-2018) to 1.84-1.96 μatm yr⁻¹ (Table 4). Within the variability in the estimations, both
595 empirical and hindcast models simulated similar growth rates in pCO₂ levels (Figure 7).

596

597 The range of sea-to-air CO₂ fluxes for the period of 1985 to 2018 was significantly different
598 for GHM (-0.48 to -0.06 PgC yr⁻¹), empirical (-0.31 to 0.03 PgC yr⁻¹) and atmospheric
599 inversion models (-0.63 to 0.09 PgC yr⁻¹) (Figure 7). The IAV trend between 1985 and 2018
600 was close for hindcast (-0.023±0.003 PgC yr⁻¹ decade⁻¹) and empirical models (-0.021±0.003
601 PgC yr⁻¹ decade⁻¹; Table 5). The trends in IAV by hindcast models between 2001 and 2018 (-
602 0.023±0.007 PgC yr⁻¹ decade⁻¹) were slightly lower compared to 1985-2000 (-0.028±0.012
603 PgC yr⁻¹ decade⁻¹) for the entire Indian Ocean suggesting the rate of sinking of CO₂ in the
604 Indian Ocean is decreasing in the recent decades. In contrast, empirical models displayed
605 larger IAV between 2001-2018 (-0.046±0.005 PgC yr⁻¹ decade⁻¹) and 1985-2000
606 (+0.007±0.007 PgC yr⁻¹ decade⁻¹). Such differences in the empirical models may come from
607 the lack of satellite Chl-a data before 1998. Therefore, the simulations of empirical models
608 may be less accurate before 1998 than after. Interestingly IAV by empirical models during
609 2001-2018 were more than double (-0.046±0.005 PgC yr⁻¹ decade⁻¹) than that of hindcast
610 models (-0.023±0.007 PgC yr⁻¹ decade⁻¹) which may be driven by variability in wind
611 products and transfer velocity coefficients used. To examine the spatial variability in IAV,
612 the same is studied in different regions of the Indian Ocean.

613

614 3.3.2. Northwestern Indian Ocean (Arabian Sea)

615

616 The pCO₂ growth of 1.64 to 1.68 μatm yr⁻¹ was simulated between 1985 and 2018 and it was
617 lower during 1985-2000 (1.32-1.41 μatm yr⁻¹) than 2001-2018 (1.76-1.88 μatm yr⁻¹) (Table 4)
618 in the Arabian Sea. The growth rates in pCO₂ levels in the Arabian Sea are close to that of the
619 atmospheric growth rate of CO₂ (WMO Bulletin; <https://gml.noaa.gov/ccgg/trends/>).

620

621 The IAV in the CO₂ fluxes by the hindcast models in the Arabian Sea was small (0.00 to 0.06
622 PgC yr⁻¹), it was larger than the mean flux to the atmosphere from 1985 to 2018 (0.03±0.01
623 PgC yr⁻¹). This suggests that the mean CO₂ flux to the atmosphere may vary significantly
624 from year to year (Figure 7).. In contrast, the atmospheric inversions (for the period 2001-
625 2018) gave a much larger standard deviation than hindcast models suggesting that about 50%
626 of the total Indian Ocean variability occurs in the NIO. The high variability in the
627 atmospheric inversions may come from the period and region of atmospheric CO₂ data used
628 in the models. The empirical models estimated lower IAV (0.03 to 0.12 PgC yr⁻¹) compared
629 to hindcast and atmospheric inversion models.

630

631 To examine the IAV trends in the recent decades, the trends between 1985-2000 and 2001-
632 2018 were compared. The IAV between 2001-2018 is lower (-0.005±0.002 PgC yr⁻¹ decade⁻¹)
633 ¹) than 1985-2000 (-0.001±0.002 PgC yr⁻¹ decade⁻¹) by hindcast models suggesting that the
634 source of the CO₂ to the atmosphere from the Arabian Sea is decreasing in the recent
635 decades. This is possible that rapid warming of the western Arabian Sea was reported in
636 recent decades (Roxy et al.,2015; Sridevi et al., 2023) resulting in weak vertical transport of
637 CO₂, and nutrients resulting in a decrease in primary production (Dunstan et al., 2018; Roxy
638 et al., 2016; Sridevi et al., 2023). A decline in Somali upwelling intensity and decreased
639 evaporation due to the weakening of winds led to the warming of the Indian Ocean was
640 reported in recent decades (D'Mello and Prasanna Kumar (2018). Sarma et al. (2000)
641 estimated that vertical mixing is the major contributor to high pCO₂ levels and fluxes to the
642 atmosphere in the Arabian Sea. The decrease in mixing may also weaken primary production
643 resulting in an increase in CO₂ flux. Recently Sridevi et al. (2023) found that net primary
644 production was decreasing only in the southern Arabian Sea (south of 12°N) whereas the
645 decrease in nutrient inputs through mixing is compensated by increased atmospheric

646 deposition of nutrients. Therefore, the weakening of upwelling intensity decreased the CO₂
647 source to the atmosphere in the past 4 decades in the Arabian Sea. The empirical models also
648 simulated a decrease in the CO₂ fluxes from $-0.002 \pm 0.002 \text{ PgC yr}^{-1} \text{ decade}^{-1}$ in 1985-2000 to
649 $-0.011 \pm 0.001 \text{ PgC yr}^{-1} \text{ decade}^{-1}$ in 2001-2018 and the magnitude of the decrease is higher
650 than hindcast models. Nevertheless, this analysis suggests that the source of CO₂ to the
651 atmosphere from the Arabian Sea is decreasing due to the warming of the basin leading to
652 stratification and a decrease in upwelling intensity in the western basin.

653

654 3.3.3. Northeastern Indian Ocean (Bay of Bengal; BoB)

655

656 The IAV trends of pCO₂ simulated by hindcast and empirical models were close (1.54 ± 0.04
657 and $1.64 \pm 0.02 \text{ } \mu\text{atm yr}^{-1}$ respectively) between 1985 and 2018 in the BoB and these rates are
658 almost close to that of in the Arabian Sea (Table 4). The pCO₂ growth rate increased between
659 1985 and 2000 ($1.34\text{-}1.46 \text{ } \mu\text{atm yr}^{-1}$) to 2001-2018 ($1.71\text{-}1.76 \text{ } \mu\text{atm yr}^{-1}$; Table 4) and it is
660 consistent with the atmospheric growth rate (<https://gml.noaa.gov/ccgg/trends/>).

661

662 The IAV in the BoB simulated by the hindcast models is small (-0.02 to $+0.02 \text{ PgC yr}^{-1}$), and
663 it is larger than the mean flux to the atmosphere from 1985 to 2018 ($0.00 \pm 0.02 \text{ PgC yr}^{-1}$).

664 This suggests that the mean CO₂ flux to the atmosphere may vary from a net weak sink to a
665 weak source to the atmosphere. The standard deviation is large suggesting that large IAV
666 occurs in the BoB. In contrast, the atmospheric inversions showed a large standard deviation
667 in comparison to hindcast models suggesting high IAV could occur in the BoB (-0.03 to
668 $+0.04 \text{ PgC yr}^{-1}$). On the opposite the empirical models showed low IAV in CO₂ fluxes (0.00
669 to 0.02 PgC yr^{-1}) and it is close to that of the annual mean flux to the atmosphere

670 (0.01±0.005 PgC yr⁻¹; Table 3). The empirical models estimated very low IAV compared to
671 hindcast and atmospheric inversion models in the BoB (Figure 7).

672

673 The IAV in the CO₂ fluxes in the BoB from the hindcast models decreased from 1985-2000 (-
674 0.002±0.002 PgC yr⁻¹ decade⁻¹) to 2001-2018 (-0.005±0.001 PgC yr⁻¹ decade⁻¹) but not
675 statistically different. (Table 5). Similarly, empirical models simulated a decrease in the
676 fluxes of CO₂ in the BoB in recent decades (Table 5). The decrease of the CO₂ sink may be
677 potentially caused by the deposition of atmospheric pollutants. Recently Sridevi and Sarma
678 (2021) analyzed long-term trends (1998-2015) in pCO₂ levels in the BoB using an empirical
679 model and noticed that pCO₂ decreased at the rate of -0.1 to -2.9 μatm yr⁻¹ in the central and
680 eastern Bay associating with the decrease in salinity. The decrease in salinity is manifested by
681 the melting of Himalayan glaciers due to climate change (Goes et al., 2020). In contrast, an
682 increase in pCO₂ levels was noticed in the head bay and western BoB (0.1 to 2.4 μatm yr⁻¹)
683 due to the deposition of atmospheric pollutants (Sarma et al., 2015; 2022). Therefore the
684 decrease in the rate of CO₂ flux from the atmosphere in the recent decade may be caused by a
685 decrease in salinity and deposition of atmospheric pollutants in the BoB.

686

687 3.3.4. Equatorial Indian Ocean (EIO)

688

689 The pCO₂ simulations displayed significant IAV by hindcast and empirical models in the
690 equatorial Indian Ocean (1.65-1.72 μatm yr⁻¹) between 1985 and 2018. The enhanced pCO₂
691 growth rate was observed during the recent decade (2001-2018; 1.52-2.01 μatm yr⁻¹; Table 4)
692 than between 1985 and 2000 (1.43-1.52 μatm yr⁻¹). The IAV in the CO₂ fluxes in the EIO
693 simulated by the hindcast models is small (-0.11 to 0.06 PgC yr⁻¹), and it is larger than the
694 mean flux to the atmosphere from 1985 to 2018 (-0.03±0.05 PgC yr⁻¹). The large standard

695 deviation in the IAV by hindcast models suggested large variations in the CO₂ fluxes in the
696 EIO and the mean CO₂ flux to the atmosphere may vary between weak sink to the source to
697 the atmosphere. In contrast, both empirical and atmospheric inversion models displayed a
698 decrease in the source for the past three decades. The hindcast models displayed a rate of
699 decrease in CO₂ fluxes from the EIO between 1985-2000 (-0.004 ± 0.005 PgC yr⁻¹ decade⁻¹)
700 to 2001-2018 (-0.006 ± 0.003 PgC yr⁻¹ decade⁻¹) whereas a decrease was also noticed by
701 empirical models but the magnitude was higher ($+0.01 \pm 0.003$ and -0.018 ± 0.002 PgC yr⁻¹
702 decade⁻¹ during 1985-2000 and 2001-2018 respectively). This analysis suggests that the CO₂
703 sink in the EIO is increasing in recent decades possibly due to the weakening of upwelling in
704 the western basin due to rapid warming (D'Mello and Prasanna Kumar, 2018; Roxy et al.,
705 2015) leading to less DIC import in surface.

706

707 3.3.5. The South Indian Ocean (SIO)

708

709 The IAV of pCO₂ simulated by hindcast and empirical models in the SIO were close
710 (1.73 ± 0.03 and 1.70 ± 0.02 $\mu\text{atm yr}^{-1}$ respectively) between 1985 and 2018. The lower pCO₂
711 growth rate was observed between 1985 and 2000 (1.43 - 1.50 $\mu\text{atm yr}^{-1}$) while increased in
712 the recent decades of 2001-2018 (1.91 - 1.98 $\mu\text{atm yr}^{-1}$ (Table 4). A slight increase in the
713 surface ocean pCO₂ growth rate from north (Arabian Sea; 1.88 ± 0.06 $\mu\text{atm yr}^{-1}$ between 2001-
714 2018) to SIO (1.98 ± 0.05 $\mu\text{atm yr}^{-1}$) was observed in the hindcast models whereas such trends
715 were not noticed in the empirical models (Table 4). In the period 1991–2007, Metzl (2009)
716 calculated an oceanic pCO₂ growth rate of 2.11 ± 0.11 $\mu\text{atm yr}^{-1}$, which is 0.4 $\mu\text{atm yr}^{-1}$ faster
717 than in the atmosphere, suggesting that this region acts as a reducing sink of atmospheric
718 CO₂. Recently Lo Monaco et al. (2021) reported increasing trends of pCO₂ in the southern
719 Mozambique Channel ranging from 1.14 $\mu\text{atm yr}^{-1}$ from 1963 to 1995, 1.70 $\mu\text{atm yr}^{-1}$ from

720 1995 to 2004 and $2.41 \mu\text{atm yr}^{-1}$ from 2004 to 2019, and these rates are close to that of
721 atmospheric CO_2 trend. The growth rate of pCO_2 estimated by both hindcast and empirical
722 models appears close to that of measured values in the SIO (Metzl, 2009; Lo Monaco et al.,
723 2021; Leseurre et al., 2022).

724

725 The IAV in the SIO by the hindcast models is small (-0.41 to $-0.03 \text{ PgC yr}^{-1}$), and it is larger
726 than the mean flux to the atmosphere from 1985 to 2018 ($-0.03 \pm 0.05 \text{ PgC yr}^{-1}$). The large
727 standard deviation in the IAV by hindcast models suggested large variations in the CO_2
728 fluxes in the SIO and the mean CO_2 flux to the atmosphere may vary between weak sink to
729 the source to the atmosphere. In contrast, the empirical model did not show large variability
730 but atmospheric inversion models displayed large standard deviations (Figure 7) with a
731 higher increase in the sink from -0.4 to $-0.45 \text{ PgC yr}^{-1}$ between 2001 and 2018. The hindcast
732 models displayed a decrease in CO_2 fluxes from the SIO between 1985-2000 (-0.02 ± 0.006
733 $\text{PgC yr}^{-1} \text{ decade}^{-1}$) to 2001-2018 ($-0.006 \pm 0.005 \text{ PgC yr}^{-1} \text{ decade}^{-1}$) whereas a decrease was
734 also noticed by empirical models but the magnitude was higher (-0.003 ± 0.005 to -
735 $0.012 \pm 0.004 \text{ PgC yr}^{-1} \text{ decade}^{-1}$ during 1985-2000 and 2001-2018 respectively).

736

737 3.4. Role of climate variability on CO_2 flux

738

739 The IAV in sea-air CO_2 fluxes in the Indian Ocean has been linked to the IOD and ENSO.
740 Valsala and Maksyutov (2013) reported a strong correlation between the IODZM and sea-air
741 CO_2 flux IAV in the Arabian Sea and that the roles of these two (ENSO and IODZM) modes
742 are complementary in the period 1985-2018. The strong IOD event occurred in 1994, 1997
743 and 2006 within the period considered in this study with a Dipole Mode Index (DMI) value
744 >0.6 . The simulated IAV by hindcast models shows an annual mean higher CO_2 flux during

745 1994, 1997 and 2006 by 9-14% in the Arabian Sea whereas a decrease by 5-30% was noticed
746 in other regions (BoB; EIO and SIO) than in adjacent years. This is consistent with earlier
747 observations (Sarma, 2006; Valsala and Maksyutov, 2013). Interestingly, empirical models
748 displayed an increase in CO₂ fluxes by 8% in 1994 but a decrease in flux by 10% was noticed
749 between 1997 and 2006 compared to the normal period in the Arabian Sea. In contrast, a
750 significant increase in CO₂ fluxes in the EIO by 3 to 45% was simulated by empirical models
751 whereas a decrease of 6-30% was simulated by hindcast models. Jabaud-Jan et al. (2004)
752 noticed sea-to-air fluxes in the subtropical zone (20°S-37°S) associated with warming in
753 January 1998, when strong IOD occurred, compared to sink observed in the same region
754 during 2000 suggesting warming induced by IOD enhanced CO₂ fluxes to the atmosphere.
755 However, neither hindcast nor empirical models captured these features. The monthly mean
756 CO₂ fluxes simulated by hindcast and empirical models in the Indian Ocean, including in the
757 Arabian Sea, did not show significant relation with Dipole Mode Index (DMI) between 1985
758 and 2018 suggesting that weak IOD may not have a significant impact on CO₂ fluxes in the
759 Indian Ocean.

760

761 The strong ENSO event (index value >1.0) occurred in 1987, 1992, 1997, 2010 and 2016
762 within the period considered in this study. During these events increase in annual mean CO₂
763 fluxes by 6-26% was observed in the Arabian Sea and BoB whereas a decrease in CO₂ fluxes
764 was noticed in the EIO and SIO by hindcast models. In contrast, empirical models showed a
765 decrease in CO₂ fluxes in the ENSO years in the Arabian Sea, BoB and SIO but an increase
766 in the EIO. The monthly ENSO index displayed a significant linear correlation with CO₂
767 fluxes by hindcast models in the Arabian Sea and BoB (p<0.001) but an insignificant
768 relationship in the EIO and SIO (p>0.01 and p>0.1 respectively) whereas insignificant
769 relation was observed with CO₂ fluxes by empirical models in all regions. Valsala and

770 Maksyutov (2013) found a positive relationship between the ENSO index and CO₂ fluxes in
771 the Arabian Sea and Southern Peninsular India. Nevertheless, this study suggests that
772 empirical models did not capture either ENSO or IOD impacts on the CO₂ fluxes in the
773 Indian Ocean.
774
775 Significant negative anomalies in the CO₂ fluxes were reported in the tropical Indian and
776 Pacific Oceans and the absence of such anomaly was reported in the Southern Ocean
777 (McKinley et al., 2020; Bennington et al., 2022). Bennington et al. (2022) reported an
778 increase in >30% of the sink after the Pinatubo eruption. Interestingly significant decrease in
779 CO₂ flux was observed between 1991 and the mean of 1992-93 in the Arabian Sea (0.038 and
780 0.032 PgC/y respectively), BoB (0.0033 and 0.002 PgC/y), EIO (-0.026 and -0.041) with
781 decrease by 16 to 57% whereas it was smaller in the case of SIO (-0.18 and -0.19 PgC/y)
782 associated with Pinatubo volcanic eruption (Fig. 7). These observations are consistent with
783 the earlier studies (McKinley et al., 2020; Bennington et al., 2022). Recently Fay et al. (2023)
784 reported high oxygen and carbon anomalies associated with Pinatubo volcanic eruptions for
785 several years in the northern and tropical Pacific and tropical Indian Ocean but an
786 insignificant impact is noticed in the Southern Ocean. The models used in this study also
787 suggest an impact of the Pinatubo volcanic eruption on Indian Ocean CO₂ fluxes around
788 1991-1992 most pronounced in the EIO region (Fig. 7).

789

790 **4. Conclusions**

791

792 The Indian Ocean is severely under-sampled with reference to surface pCO₂ levels. In order
793 to estimate the uptake of CO₂ by the Indian Ocean, CO₂ fluxes were simulated using several
794 approaches, such as a) hindcast, b) atmospheric inversions, and c) empirical models, were

795 analyzed at different time scales and compared with spatially interpolated observations
796 (called climatology). Our study suggests that the annual mean CO₂ uptake by the entire
797 Indian Ocean (north of 37.5°S) from all approaches varied between -0.27 and -0.13 PgC yr⁻¹
798 with a mean value of all models of -0.19±0.01 PgC yr⁻¹. The SIO (south of 18°S) region is a
799 dominant annual sink for the atmospheric CO₂ with a mean of all models of -0.23±0.11 PgC
800 yr⁻¹. In contrast, a mild source of CO₂ in the atmosphere was simulated by all models
801 (0.02±0.05 PgC yr⁻¹) in the north of 18°S. The estimation of CO₂ uptake by the Indian Ocean
802 was shown little variations among models.

803

804 All models simulated spatial variability in CO₂ fluxes in the Indian Ocean except for the
805 underestimation of upwelling fluxes off Oman/Somalia coasts, and the EIO and
806 overestimation of sink in the BoB due to poor monsoon mixing and freshwater discharge
807 simulations in the hindcast models. The RHM have improved the simulation of CO₂ fluxes,
808 compared to GHM, in these regions but has not reached close to the climatology. Variations
809 in CO₂ fluxes by different models were also driven by variations in wind products, transfer
810 velocity parameterization and atmospheric CO₂ data used in the flux estimations.

811

812 The atmospheric growth rate of pCO₂ was well simulated by all models and they captured the
813 seasonal cycle in the sea-air CO₂ fluxes, however, the stronger amplitudes were simulated by
814 all models than climatology. The empirical models simulated the seasonal cycle of sea-air
815 CO₂ fluxes reasonably well with the observations. The difference between the hindcast and
816 atmospheric inversion models and also in comparison with climatology may reflect errors in
817 the model formulations and also poor observational data both in the atmosphere and ocean
818 surface.

819

820 The inter-annual variability in CO₂ fluxes by the hindcast models is relatively weaker
821 compared to the atmospheric inversions. The hindcast models suggest a slight weakening of
822 the sink over the period of 1985-2018 in the SIO. In contrast, a decrease in the source of CO₂
823 in the atmosphere was simulated in the Arabian Sea, BoB and EIO by the hindcast and
824 empirical models. It is difficult to conclude how models are performing about IAV due to the
825 lack of time-series atmospheric and surface ocean pCO₂ observations. All models projected
826 the influence of atmospheric extreme events, such as IODZM and ENSO on CO₂ fluxes in the
827 Indian Ocean.

828

829 Unless the monsoon mixing is represented well in the models, it will remain difficult to
830 confidently project the future changes in CO₂ fluxes in the Indian Ocean. The lack of
831 seasonal data in most parts of the Indian Ocean is another serious problem to validate the
832 models. Significant improvement in model performance was not noticed since the RECCAP1
833 comparison between models and observations due to the lack of addition of new data in this
834 region (Sarma et al., 2013). Therefore, intensive ocean observations of pCO₂ and atmospheric
835 tower observations are required for further improvements of the models.

836

837 The Indian Ocean experiences extreme events such as eddies (Chen et al., 2012) and tropical
838 cyclones and both cause enormous effluxes of CO₂ to the atmosphere that would influence
839 local CO₂ fluxes (Byju and Prasanna Kumar, 2011; Ye et al., 2019). Swapna et al. (2022)
840 projected an increase in cyclonic activity in the future in the Indian Ocean that may result in
841 enhanced CO₂ fluxes at the air-sea interface. High resolution, with reference to space and
842 time, is required to capture such features. The regional models are highly useful to capture
843 such signatures than global models. It would be interesting to segregate the contribution of
844 CO₂ fluxes due to an increase in cyclonic activity due to climate change.

845

846 Rapid warming of the Indian Ocean (Roxy et al., 2015) is experiencing and began to play an
847 important role in global ocean heat uptake (Li et al, 2018). The decrease in the rate of
848 warming due to aerosols was reported in the northern Indian Ocean (Sridevi et al., 2023). The
849 decrease in the primary production in the western Indian Ocean (Roxy et al., 2016;
850 Dalpadado et al., 2021; Sridevi et al., 2023), was reported due to the decline in wind speed
851 and upwelling intensity. The lack of primary productivity trends due to an increase in the
852 deposition of nutrients from the atmosphere was reported (Sarma et al., 2022; Sridevi et al.,
853 2023). Rapid rate of ocean acidification was reported due to the atmospheric deposition of
854 pollutants (Sarma et al., 2015; 2021; Kumar et al., 2022). Therefore the inclusion of
855 atmospheric pollutants in the model improves the simulations of future changes in CO₂ fluxes
856 significantly. Evaluating the changes in possible drivers due to climate change would be an
857 interesting issue to look into in the future.

858

859 One serious drawback in the present study to use of observational climatology of CO₂ fluxes
860 to compare with the model simulations. Due to a lack of observational data in the Indian
861 Ocean, inter and extrapolations were done based on the advection-diffusion model
862 (Takahashi et al., 2009). Recently Davis and Goyet (2021) suggested a new method to fill the
863 gaps to balance the error in the undersampled regions. Utilizing such tools, as shown by
864 Guglielmi et al. (2022 a, b), may further decrease errors associated with climatology and the
865 evaluation of model simulations will be enhanced.

866

867 **Acknowledgement:** We would like to thank all the modellers who have supplied the model
868 outcomes to perform this analysis. The RECCAP2 organizers are also thanked for organizing
869 the meeting in Japan and also simulating discussions over the online platform to perform this
870 exercise, especially Drs. Jensdaniel Mueller, Nicolas Gruber. NC is supported by the Arctic

871 Challenge for Sustainability phase II (ArCS-II; JPMXD1420318865) Projects of the Ministry
872 of Education, Culture, Sports, Science and Technology (MEXT). PKP is partly supported by
873 the Environment Research and Technology Development Fund (JPMEERF21S20800) of the
874 Environmental Restoration and Conservation Agency of Japan. The INCOIS-BIO-ROMS
875 regional Indian Ocean model has been configured as a part of the ‘Development of Climate
876 Change Advisory Services’ project of the Indian National Centre for Ocean Information
877 Services (INCOIS) under the ‘Deep Ocean Mission’ programme of the Ministry of Earth
878 Sciences (MoES). This is INCOIS contribution number XXX. ZL is supported by Tamkeen
879 through Research Institute grant CG009 to the NYUAD Arabian Center for Climate and
880 Environmental Sciences (ACCESS). The Surface Ocean CO₂ Atlas (SOCAT,
881 www.socat.info) used for empirical models is an international effort, endorsed by the
882 International Ocean Carbon Coordination Project (IOCCP), the Surface Ocean Lower
883 Atmosphere Study (SOLAS) and the Integrated Marine Biogeochemistry and Ecosystem
884 Research program (IMBER), to deliver a uniformly quality-controlled surface ocean CO₂
885 database. We thank the two anonymous reviewers for making constructive suggestions,
886 which resulted in improvements to this paper. This is NIO contribution number

887

888

889 References

- 890 Al Azhar, M., Lachkar, Z., Lévy, M., & Smith, S. (2017). Oxygen minimum zone contrasts
 891 between the Arabian Sea and the Bay of Bengal implied by differences in remineralization
 892 depth. *Geophysical Research Letters*, 44(21), 11-106.
- 893 Bakker, D. C., Pfeil, B., Landa, C. S., Metzl, N., O'brien, K. M., Olsen, A., et al. (2016). A
 894 multi-decade record of high-quality fCO₂ data in version 3 of the Surface Ocean CO₂ Atlas
 895 (SOCAT). *Earth System Science Data*, 8(2), 383-413.
- 896 Bakker, D. C., Pfeil, B., Smith, K., Hankin, S., Olsen, A., Alin, S. R., et al. (2014). An update
 897 to the Surface Ocean CO₂ Atlas (SOCAT version 2). *Earth System Science Data*, 6(1), 69-
 898 90.
- 899 Bakker, D. C. E., Alin, S. R., Bates, N., Becker, M., Castaño-Primo, R., Cosca, C. E., et al.
 900 (2020). Surface Ocean CO₂ Atlas Database Version 2020 (SOCATv2020)(NCEI accession
 901 0210711). *NOAA National Centers for Environmental Information*. [Doi.org/10.25921/4xkx-ss49](https://doi.org/10.25921/4xkx-ss49). 2020.
- 903 Bates, N. R., Pequignet, A. C., & Sabine, C. L. (2006). Ocean carbon cycling in the Indian
 904 Ocean: 1. Spatiotemporal variability of inorganic carbon and air-sea CO₂ gas
 905 exchange. *Global Biogeochemical Cycles*, 20(3).
- 906 Behrenfeld, M. J., & Falkowski, P. G. (1997). Photosynthetic rates derived from satellite-
 907 based chlorophyll concentration. *Limnology and oceanography*, 42(1), 1-20.
- 908 Bennington, V., Gloege, L., & McKinley, G. A. (2022). Variability in the global ocean
 909 carbon sink from 1959 to 2020 by correcting models with observations. *Geophysical
 910 Research Letters*, 49(14), e2022GL098632.
- 911 Bettencourt, J. H., López, C., Hernández-García, E., Montes, I., Sudre, J., Dewitte, B., et al.
 912 (2015). Boundaries of the Peruvian oxygen minimum zone shaped by coherent mesoscale
 913 dynamics. *Nature Geoscience*, 8(12), 937-940.
- 914 Bopp, L., Resplandy, L., Orr, J. C., Doney, S. C., Dunne, J. P., Gehlen, M., ... & Vichi, M.
 915 (2013). Multiple stressors of ocean ecosystems in the 21st century: projections with CMIP5
 916 models. *Biogeosciences*, 10(10), 6225-6245.
- 917 Brandt, P., Bange, H. W., Banyte, D., Dengler, M., Didwischus, S. H., Fischer, T., et al.
 918 (2015). On the role of circulation and mixing in the ventilation of oxygen minimum zones
 919 with a focus on the eastern tropical North Atlantic. *Biogeosciences*, 12(2), 489-512.
- 920 Byju, P., & Kumar, S. P. (2011). Physical and biological response of the Arabian Sea to
 921 tropical cyclone Phyan and its implications. *Marine Environmental Research*, 71(5), 325-330.
- 922 Canadell, J.G., P.M.S. Monteiro, et al. 2021. Global Carbon and other Biogeochemical
 923 Cycles and Feedbacks., in *Climate Change 2021: The Physical Science Basis*. Contribution of
 924 Working Group I to the Sixth Assessment Report of the Intergovernmental Panel on Climate
 925 Change, edited by L. G. Masson-Delmotte et al., Cambridge University Press.
- 926 Chakraborty, K., Valsala, V., Bhattacharya, T., & Ghosh, J. (2021). Seasonal cycle of surface
 927 ocean pCO₂ and pH in the northern Indian Ocean and their controlling factors. *Progress in
 928 Oceanography*, 198, 102683.
- 929 Chakraborty, K., Kumar, N., Girishkumar, M. S., Gupta, G. V. M., Ghosh, J., Udaya
 930 Bhaskar, T. V. S., & Thangaprakash, V. P. (2019). Assessment of the impact of spatial

931 resolution on ROMS simulated upper-ocean biogeochemistry of the Arabian Sea from an
932 operational perspective. *Journal of Operational Oceanography*, 12(2), 116-142.

933 Chakraborty, K., Valsala, V., Gupta, G. V. M., & Sarma, V. V. S. S. (2018). Dominant
934 biological control over upwelling on pCO₂ in sea east of Sri Lanka. *Journal of Geophysical*
935 *Research: Biogeosciences*, 123(10), 3250-3261.

936 Chandra, N., Patra, P. K., Niwa, Y., Ito, A., Iida, Y., Goto, D., et al. (2022). Estimated
937 regional CO₂ flux and uncertainty based on an ensemble of atmospheric CO₂
938 inversions. *Atmospheric Chemistry and Physics*, 22(14), 9215-9243.

939 Chau, T. T. T., Gehlen, M., & Chevallier, F. (2022). A seamless ensemble-based
940 reconstruction of surface ocean pCO₂ and air–sea CO₂ fluxes over the global coastal and
941 open oceans. *Biogeosciences*, 19(4), 1087-1109.

942
943 Chen, G., Wang, D., & Hou, Y., (2012). The features and interannual variability mechanism
944 of mesoscale eddies in the Bay of Bengal. *Continental Shelf Research*. 47, 178–185.

945 Chevallier, F., Fisher, M., Peylin, P., Serrar, S., Bousquet, P., Bréon, F. M., et al. (2005).
946 Inferring CO₂ sources and sinks from satellite observations: Method and application to
947 TOVS data. *Journal of Geophysical Research: Atmospheres*, 110(D24).

948 Cocco, V., Joos, F., Steinacher, M., Frölicher, T. L., Bopp, L., Dunne, J., et al. (2013).
949 Oxygen and indicators of stress for marine life in multi-model global warming projections.
950 *Biogeosciences*, 10(3), 1849-1868.

951 Dalpadado, P., Arrigo, K. R., van Dijken, G. L., Gunasekara, S. S., Ostrowski, M., Bianchi,
952 G., & Sperfeld, E. (2021). Warming of the Indian Ocean and its impact on temporal and
953 spatial dynamics of primary production. *Progress in Oceanography*, 198, 102688.

954 De Verneil, A., Lachkar, Z., Smith, S., & Lévy, M. (2022). Evaluating the Arabian Sea as a
955 regional source of atmospheric CO₂: seasonal variability and drivers. *Biogeosciences*, 19(3),
956 907-929.

957 D'Mello, J. R., & Prasanna Kumar, S. (2018). Processes controlling the accelerated warming
958 of the Arabian Sea. *International Journal of Climatology*, 38(2), 1074-1086.

959 Davis, D., and Goyet, C. 2021. Balanced error sampling with applications to ocean
960 biogeochemical sampling, University of Perpignan, France, pp. 214.

961 Dunstan, P. K., Foster, S. D., King, E., Risbey, J., O’Kane, T. J., Monselesan, D., et al.
962 (2018). Global patterns of change and variation in sea surface temperature and chlorophyll
963 a. *Scientific reports*, 8(1), 1-9.

964 Fay, A. R., Gregor, L., Landschützer, P., McKinley, G. A., Gruber, N., Gehlen, M., et al.
965 (2021). SeaFlux: harmonization of air–sea CO₂ fluxes from surface pCO₂ data products
966 using a standardized approach. *Earth System Science Data*, 13(10), 4693-4710.

967 Fay, A.R., McKinley, G.A., Lovenduski, N.S., Eddebbar, Y., Levy, M.N., Long, M.C.,
968 Olivarez, H.C., & Rustagi, R.R. (2023). Immediate and long-lasting impacts of the Mt.
969 Pinatubo Eruption on Ocean oxygen and carbon inventories. *Global Biogeochemical Cycles*,
970 37, e2022GB007513.

971 Friedlingstein, P., Jones, M. W., O'Sullivan, M., Andrew, R. M., Bakker, D. C., Hauck, J., et
972 al. (2022). Global carbon budget 2021. *Earth System Science Data*, 14(4), 1917-2005.

973 George, M. D., Kumar, M. D., Naqvi, S. W. A., Banerjee, S., Narvekar, P. V., De Sousa, S.
974 N., et al. (1994). A study of the carbon dioxide system in the northern Indian Ocean during
975 premonsoon. *Marine Chemistry*, 47(3-4), 243-254.

976 Ghosh, S., Sinha, P., Bhatla, R., Mall, R. K., & Sarkar, A. (2022). Assessment of Lead-Lag
977 and Spatial Changes in simulating different epochs of the Indian summer monsoon using
978 RegCM4. *Atmospheric Research*, 265, 105892.

979 Ghosh, J., Chakraborty, K., Bhattacharya, T., Valsala, V., & Baduru, B. (2022). Impact of
980 coastal upwelling dynamics on the pCO₂ variability in the southeastern Arabian Sea.
981 *Progress in Oceanography*, 203, 102785.

982 Gloege, L., Yan, M., Zheng, T., & McKinley, G. A. (2022). Improved quantification of ocean
983 carbon uptake by using machine learning to merge global models and pCO₂ data. *Journal of*
984 *Advances in Modeling Earth Systems*, 14(2), e2021MS002620.

985 Goes, J. I., Tian, H., Gomes, H. D. R., Anderson, O. R., Al-Hashmi, K., deRada, S., et al.
986 (2020). Ecosystem state change in the Arabian Sea fuelled by the recent loss of snow over the
987 Himalayan-Tibetan plateau region. *Scientific reports*, 10(1), 1-8.

988 Goyet, C., Millero, F. J., O'Sullivan, D. W., Eiseheid, G., McCue, S. J., & Bellerby, R. G. J.
989 (1998). Temporal variations of pCO₂ in surface seawater of the Arabian Sea in 1995. *Deep*
990 *Sea Research Part I: Oceanographic Research Papers*, 45(4-5), 609-623.

991 Gregor, L., Lebehot, A. D., Kok, S., & Scheel Monteiro, P. M. (2019). A comparative
992 assessment of the uncertainties of global surface ocean CO₂ estimates using a machine-
993 learning ensemble (CSIR-ML6 version 2019a)—have we hit the wall?. *Geoscientific Model*
994 *Development*, 12(12), 5113-5136.

995 Gregor, L., & Gruber, N. (2021). OceanSODA-ETHZ: a global gridded data set of the surface
996 ocean carbonate system for seasonal to decadal studies of ocean acidification. *Earth System*
997 *Science Data*, 13(2), 777-808.

998 Gruber, N., Gloor, M., Mikaloff Fletcher, S. E., Doney, S. C., Dutkiewicz, S., Follows, M. J.,
999 et al. (2009). Oceanic sources, sinks, and transport of atmospheric CO₂. *Global*
1000 *biogeochemical cycles*, 23(1).

1001 Guglielmi V., F. Touratier, C. Goyet (2022a). Design of sampling strategy measurements of
1002 CO₂/carbonate properties. *Journal of Oceanography and Aquaculture*, 6(3):
1003 000227. [doi:10.23880/ijoac-16000227](https://doi.org/10.23880/ijoac-16000227)

1004 Guglielmi V., F. Touratier, C. Goyet (2022b). Determination of discrete sampling locations
1005 minimizing both the number of samples and the maximum interpolation error: application to
1006 measurements of surface ocean properties. *Journal of Sea Research*, in revision

1007 Iida, Y., Takatani, Y., Kojima, A., & Ishii, M. (2021). Global trends of ocean CO₂ sink and
1008 ocean acidification: an observation-based reconstruction of surface ocean inorganic carbon
1009 variables. *Journal of Oceanography*, 77(2), 323-358.

1010 Jabaud-Jan, A., Metzl, N., Brunet, C., Poisson, A., & Schauer, B. (2004). Interannual
1011 variability of the carbon dioxide system in the southern Indian Ocean (20 S–60 S): The
1012 impact of a warm anomaly in austral summer 1998. *Global Biogeochemical Cycles*, 18(1).

1013 Körtzinger, A., Duinker, J. C., & Mintrop, L. (1997). Strong CO₂ emissions from the Arabian
1014 Sea during south-west monsoon. *Geophysical Research Letters*, 24(14), 1763-1766.

- 1015 Kumar, M. D., Naqvi, S. W. A., George, M. D., & Jayakumar, D. A. (1996). A sink for
1016 atmospheric carbon dioxide in the northeast Indian Ocean. *Journal of Geophysical Research:*
1017 *Oceans*, 101(C8), 18121-18125.
- 1018 Kumari, V. R., Sarma, V. V. S. S., Mahesh, G., & Sudheer, A. K. (2022). Temporal
1019 variations in the chemical composition of aerosols over the coastal Bay of
1020 Bengal. *Atmospheric Pollution Research*, 13(2), 101300.
- 1021 Kumari, V.R., Sarma, V.V.S.S. & Dileep Kumar, M. (2022). Spatial variability in aerosol
1022 composition and its seawater acidification potential in coastal waters of the western coastal
1023 Bay of Bengal. *Journal of Earth System Science*, doi.org/10.1007/s12040-022-01996-w.
- 1024 Kumari, V. R., Yadav, K., Sarma, V. V. S. S., & Dileep Kumar, M. (2021). Acidification of
1025 the coastal Bay of Bengal by aerosols deposition. *Journal of Earth System Science*, 130(4), 1-
1026 13.
- 1027 Kwiatkowski, L., Torres, O., Bopp, L., Aumont, O., Chamberlain, M., Christian, J. R., et al.,
1028 (2020). Twenty-first century ocean warming, acidification, deoxygenation, and upper-ocean
1029 nutrient and primary production decline from CMIP6 model projections. *Biogeosciences*,
1030 17(13), 3439-3470.
- 1031 Lachkar, Z., Lévy, M., & Smith, S. (2018). Intensification and deepening of the Arabian Sea
1032 oxygen minimum zone in response to increase in Indian monsoon wind intensity.
1033 *Biogeosciences*, 15(1), 159-186.
- 1034 Lachkar, Z., Mehari, M., Al Azhar, M., Lévy, M., & Smith, S. (2021). Fast local warming is
1035 the main driver of recent deoxygenation in the northern Arabian Sea. *Biogeosciences*, 18(20),
1036 5831-5849.
- 1037 Lachkar, Z., Smith, S., Lévy, M., & Pauluis, O. (2016). Eddies reduce denitrification and
1038 compress habitats in the Arabian Sea. *Geophysical Research Letters*, 43(17), 9148-9156.
- 1039 Landschützer, P., Gruber, N., & Bakker, D. C. (2016). Decadal variations and trends of the
1040 global ocean carbon sink. *Global Biogeochemical Cycles*, 30(10), 1396-1417.
- 1041 Lauvset, S. K., Gruber, N., Landschützer, P., Olsen, A., & Tjiputra, J. (2015). Trends and
1042 drivers in global surface ocean pH over the past 3 decades. *Biogeosciences*, 12(5), 1285-
1043 1298.
- 1044 Leseurre, C., Lo Monaco, C., Reverdin, G., Metzl, N., Fin, J., Mignon, C., & Benito, L.
1045 (2022). Summer trends and drivers of sea surface fCO₂ and pH changes observed in the
1046 southern Indian Ocean over the last two decades (1998–2019). *Biogeosciences*, 19(10), 2599-
1047 2625.
- 1048 Li, Y., Han, W., Hu, A., Meehl, G. A., & Wang, F. (2018). Multidecadal changes of the
1049 upper Indian Ocean heat content during 1965–2016. *Journal of Climate*, 31(19), 7863-7884.
- 1050 Landschützer, P., Gruber, N., & Bakker, D. C. (2016). Decadal variations and trends of the
1051 global ocean carbon sink. *Global Biogeochemical Cycles*, 30(10), 1396-1417.
- 1052 Louanchi, F., Metzl, N., & Poisson, A. (1996). Modelling the monthly sea surface fCO₂
1053 fields in the Indian Ocean. *Marine Chemistry*, 55(3-4), 265-279.
- 1054 Lo Monaco, C., Metzl, N., Fin, J., Mignon, C., Cuet, P., Douville, É., ... & Tribollet, A.
1055 (2021). Distribution and long-term change of the sea surface carbonate system in the
1056 Mozambique Channel (1963–2019). *Deep Sea Research Part II: Topical Studies in*
1057 *Oceanography*, 186, 104936.

- 1058 McKinley, G. A., Fay, A. R., Eddebbbar, Y. A., Gloege, L., & Lovenduski, N. S. (2020).
 1059 External forcing explains recent decadal variability of the ocean carbon sink. *AGU*
 1060 *Advances*, 1(2), e2019AV000149.
- 1061 Metzl, N. (2009). Decadal increase of oceanic carbon dioxide in Southern Indian Ocean
 1062 surface waters (1991–2007). *Deep Sea Research Part II: Topical Studies in*
 1063 *Oceanography*, 56(8-10), 607-619.
- 1064 Metzl, N., Beauverger, C., Brunet, C., Goyet, C., & Poisson, A. (1991). Surface water carbon
 1065 dioxide in the southwest Indian sector of the Southern Ocean: a highly variable CO₂
 1066 source/sink region in summer. *Marine Chemistry*, 35(1-4), 85-95.
- 1067 Metzl, N., Lo Monaco, C., Leseurre, C., Ridame, C., Fin, J., Mignon, C., et al. (2022). The
 1068 impact of the South-East Madagascar Bloom on the oceanic CO₂
 1069 sink. *Biogeosciences*, 19(5), 1451-1468.
- 1070 Metzl, N., Louanchi, F., & Poisson, A. (1998). Seasonal and interannual variations of sea
 1071 surface carbon dioxide in the subtropical Indian Ocean. *Marine Chemistry*, 60(1-2), 131-146.
- 1072 Metzl, N., Poisson, A., Louanchi, F., Brunet, C., Schauer, B., & Bres, B. (1995). Spatio-
 1073 temporal distributions of air-sea fluxes of CO₂ in the Indian and Antarctic Oceans: A first
 1074 step. *Tellus B*, 47(1-2), 56-69.
- 1075 Millero, F. J., Degler, E. A., O'Sullivan, D. W., Goyet, C., & Eiseid, G. (1998). The carbon
 1076 dioxide system in the Arabian Sea. *Deep Sea Research Part II: Topical Studies in*
 1077 *Oceanography*, 45(10-11), 2225-2252.
- 1078 Miyama, T., Kominami, Y., Tamai, K., Nobuhiro, T., & Goto, Y. (2003). Automated foliage
 1079 chamber method for long-term measurement of CO₂ flux in the uppermost canopy. *Tellus B:*
 1080 *Chemical and Physical Meteorology*, 55(2), 322-330.
- 1081 Mukhopadhyay, S. K., Biswas, H., De, T. K., Sen, S., & Jana, T. K. (2002). Seasonal effects
 1082 on the air–water carbon dioxide exchange in the Hooghly estuary, NE coast of Bay of
 1083 Bengal, India. *Journal of Environmental Monitoring*, 4(4), 549-552.
- 1084 Murtugudde, R., & Busalacchi, A. J. (1999). Interannual variability of the dynamics and
 1085 thermodynamics of the tropical Indian Ocean. *Journal of Climate*, 12(8), 2300-2326.
- 1086 Murtugudde, R., McCreary Jr, J. P., & Busalacchi, A. J. (2000). Oceanic processes associated
 1087 with anomalous events in the Indian Ocean with relevance to 1997–1998. *Journal of*
 1088 *Geophysical Research: Oceans*, 105(C2), 3295-3306.
- 1089 Papa, F., Bala, S. K., Pandey, R. K., Durand, F., Gopalakrishna, V. V., Rahman, A.,
 1090 & Rossow, W. B. (2012). Ganga-Brahmaputra river discharge from Jason-2 radar altimetry:
 1091 an update to the long-term satellite-derived estimates of continental freshwater forcing flux
 1092 into the Bay of Bengal. *Journal of Geophysical Research: Oceans*, 117(C11).
- 1093 Pfeil, B., Olsen, A., Bakker, D. C., Hankin, S., Koyuk, H., Kozyr, A., et al. (2013). A
 1094 uniform, quality controlled Surface Ocean CO₂ Atlas (SOCAT). *Earth System Science*
 1095 *Data*, 5(1), 125-143.
- 1096 Poisson, A., Metzl, N., Brunet, C., Schauer, B., Bres, B., Ruiz-Pino, D., & Louanchi, F.
 1097 (1993). Variability of sources and sinks of CO₂ in the Western Indian and Southern Oceans
 1098 during the year 1991. *Journal of Geophysical Research: Oceans*, 98(C12), 22759-22778.
- 1099 Rödenbeck, C., Bakker, D. C., Gruber, N., Iida, Y., Jacobson, A. R., Jones, S., et al. (2015).
 1100 Data-based estimates of the ocean carbon sink variability—first results of the Surface Ocean
 1101 pCO₂ Mapping intercomparison (SOCOM). *Biogeosciences*, 12(23), 7251-7278.

- 1102 Rödenbeck, C., Keeling, R. F., Bakker, D. C., Metzl, N., Olsen, A., Sabine, C., & Heimann,
1103 M. (2013). Global surface-ocean p CO₂ and sea–air CO₂ flux variability from an
1104 observation-driven ocean mixed-layer scheme. *Ocean Science*, 9(2), 193-216.
- 1105 Roxy, M. K., Modi, A., Murtugudde, R., Valsala, V., Panickal, S., Prasanna Kumar, S., et al.
1106 (2016). A reduction in marine primary productivity driven by rapid warming over the tropical
1107 Indian Ocean. *Geophysical Research Letters*, 43(2), 826-833.
- 1108 Roxy, M. K., Ritika, K., Terray, P., Murtugudde, R., Ashok, K., & Goswami, B. N. (2015).
1109 Drying of Indian subcontinent by rapid Indian Ocean warming and a weakening land-sea
1110 thermal gradient. *Nature communications*, 6(1), 1-10.
- 1111 Sabine, C. L., Key, R. M., Johnson, K. M., Millero, F. J., Poisson, A., Sarmiento, J. L., et al.
1112 (1999). Anthropogenic CO₂ inventory of the Indian Ocean. *Global Biogeochemical*
1113 *Cycles*, 13(1), 179-198.
- 1114 Sabine, C. L., Wanninkhof, R., Key, R. M., Goyet, C., & Millero, F. J. (2000). Seasonal CO₂
1115 fluxes in the tropical and subtropical Indian Ocean. *Marine Chemistry*, 72(1), 33-53.
- 1116 Saji, N. H., Goswami, B. N., Vinayachandran, P. N., & Yamagata, T. (1999). A dipole mode
1117 in the tropical Indian Ocean. *Nature*, 401(6751), 360-363.
- 1118 Sarma, V. V. S. S., Swathi, P. S., Kumar, M. D., Prasannakumar, S., Bhattathiri, P. M. A.,
1119 Madhupratap, M., et al. (2003). Carbon budget in the eastern and central Arabian Sea: An
1120 Indian JGOFS synthesis. *Global Biogeochemical Cycles*, 17(4).
- 1121 Sarma, V. V. S. S. (2003). Monthly variability in surface pCO₂ and net air-sea CO₂ flux in
1122 the Arabian Sea. *Journal of Geophysical Research: Oceans*, 108(C8).
- 1123 Sarma, V. V. S. S. (2006). The influence of Indian Ocean Dipole (IOD) on biogeochemistry
1124 of carbon in the Arabian Sea during 1997–1998. *Journal of earth system science*, 115(4),
1125 433-450.
- 1126 Sarma, V. V. S. S., Krishna, M. S., & Srinivas, T. N. R. (2020). Sources of organic matter
1127 and tracing of nutrient pollution in the coastal Bay of Bengal. *Marine Pollution Bulletin*, 159,
1128 111477.
- 1129 Sarma, V. V. S. S., Krishna, M. S., Paul, Y. S., & Murty, V. S. N. (2015). Observed changes
1130 in ocean acidity and carbon dioxide exchange in the coastal Bay of Bengal—a link to air
1131 pollution. *Tellus B: Chemical and Physical Meteorology*, 67(1), 24638.
- 1132 Sarma, V. V. S. S., Krishna, M. S., Rao, V. D., Viswanadham, R., Kumar, N. A., Kumari, T.
1133 R., et al. (2012). Sources and sinks of CO₂ in the west coast of Bay of Bengal. *Tellus B:*
1134 *Chemical and Physical Meteorology*, 64(1), 10961.
- 1135 Sarma, V. V. S. S., Krishna, M. S., Srinivas, T. N. R., Kumari, V. R., Yadav, K., & Kumar,
1136 M. D. (2021). Elevated acidification rates due to deposition of atmospheric pollutants in the
1137 coastal Bay of Bengal. *Geophysical Research Letters*, 48(16), e2021GL095159.
- 1138 Sarma, V. V. S. S., Kumar, G. S., Yadav, K., Dalabehera, H. B., Rao, D. N., Behera, S., &
1139 Loganathan, J. (2019). Impact of eddies on dissolved inorganic carbon components in the
1140 Bay of Bengal. *Deep Sea Research Part I: Oceanographic Research Papers*, 147, 111-120.
- 1141 Sarma, V. V. S. S., Kumar, M. D., & George, M. D. (1998). The central and eastern Arabian
1142 Sea as a perennial source of atmospheric carbon dioxide. *Tellus B: Chemical and Physical*
1143 *Meteorology*, 50(2), 179-184.

- 1144 Sarma, V. V. S. S., Kumar, M. D., Gauns, M., & Madhupratap, M. (2000). Seasonal controls
1145 on surface pCO₂ in the central and eastern Arabian Sea. *Journal of Earth System*
1146 *Science*, 109(4), 471-479.
- 1147 Sarma, V. V. S. S., Kumar, M. D., George, M. D., & Rajendran, A. (1996). Seasonal
1148 variations in inorganic carbon components in the central and eastern Arabian Sea. *Current*
1149 *Science*, 852-856.
- 1150 Sarma, V. V. S. S., Kumari, V. R., Srinivas, T. N. R., Krishna, M. S., Ganapathi, P., & Murty,
1151 V. S. N. (2018). East India Coastal Current controls the dissolved inorganic carbon in the
1152 coastal Bay of Bengal. *Marine Chemistry*, 205, 37-47.
- 1153 Sarma, V. V. S. S., Lenton, A., Law, R. M., Metzl, N., Patra, P. K., Doney, S., et al. (2013).
1154 Sea-air CO₂ fluxes in the Indian Ocean between 1990 and 2009. *Biogeosciences*, 10(11),
1155 7035-7052.
- 1156 Sarma, V. V. S. S., Prasad, M. H. K., & Dalabehera, H. B. (2021). Influence of phytoplankton
1157 pigment composition and primary production on pCO₂ levels in the Indian Ocean. *Journal of*
1158 *Earth System Science*, 130(2), 1-16.
- 1159 Sarma, V. V. S. S., Rao, G. D., Viswanadham, R., Sherin, C. K., Salisbury, J., Omand, M.
1160 M., et al. (2016). Effects of freshwater stratification on nutrients, dissolved oxygen, and
1161 phytoplankton in the Bay of Bengal. *Oceanography*, 29(2), 222-231.
- 1162 Schott, F. A., & McCreary Jr, J. P. (2001). The monsoon circulation of the Indian
1163 Ocean. *Progress in Oceanography*, 51(1), 1-123.
- 1164 Schott, F. A., Dengler, M., & Schoenefeldt, R. (2002). The shallow overturning circulation of
1165 the Indian Ocean. *Progress in oceanography*, 53(1), 57-103.
- 1166 Schott, F. A., Xie, S. P., & McCreary Jr, J. P. (2009). Indian Ocean circulation and climate
1167 variability. *Reviews of Geophysics*, 47(1).
- 1168 Sridevi, B., & Sarma, V. V. S. S. (2021). Role of river discharge and warming on ocean
1169 acidification and pCO₂ levels in the Bay of Bengal. *Tellus B: Chemical and Physical*
1170 *Meteorology*, 73(1), 1-20.
- 1171 Sridevi, B, Sabira, Sk., & Sarma, V.V.S.S. (2023). Impact of ocean warming on net primary
1172 production in the northern Indian Ocean: role of aerosols and freshening of surface ocean.
1173 *Environmental Science and Pollution Research*, doi: 10.1007/s11356-023-26001-9.
- 1174 Sutton, A. J., Feely, R. A., Maenner-Jones, S., Musielwicz, S., Osborne, J., Dietrich, C.,
1175 Monacci, N., Cross, J., Bott, R., Kozyr, A., Andersson, A. J., Bates, N. R., Cai, W.-J., Cronin,
1176 M. F., De Carlo, E. H., Hales, B., Howden, S. D., Lee, C. M., Manzello, D. P., McPhaden, M.
1177 J., Meléndez, M., Mickett, J. B., Newton, J. A., Noakes, S. E., Noh, J. H., Olafsdottir, S. R.,
1178 Salisbury, J. E., Send, U., Trull, T. W., Vandemark, D. C., and Weller, R. A. (2019)
1179 Autonomous seawater pCO₂ and pH time series from 40 surface buoys and the emergence of
1180 anthropogenic trends, *Earth Syst. Sci. Data*, 11, 421-439, [https://doi.org/10.5194/essd-11-](https://doi.org/10.5194/essd-11-421-2019)
1181 [421-2019](https://doi.org/10.5194/essd-11-421-2019).
- 1182 Swapna, P., Sreeraj, P., Sandeep, N., Jyoti, J., Krishnan, R., Prajeesh, A. G., et al. (2022).
1183 Increasing frequency of extremely severe cyclonic storms in the north Indian Ocean by
1184 anthropogenic warming and southwest monsoon weakening. *Geophysical Research Letters*,
1185 49(3), e2021GL094650.
- 1186 Takahashi, T., Sutherland, S. C., Wanninkhof, R., Sweeney, C., Feely, R. A., Chipman, D.
1187 W., et al. (2009). Climatological mean and decadal change in surface ocean pCO₂, and net

- 1188 sea–air CO₂ flux over the global oceans. *Deep Sea Research Part II: Topical Studies in*
1189 *Oceanography*, 56(8-10), 554-577.
- 1190 Thompson, D. W., & Solomon, S. (2002). Interpretation of recent Southern Hemisphere
1191 climate change. *Science*, 296(5569), 895-899.
- 1192 Valsala, V., & Maksyutov, S. (2013). Interannual variability of the air–sea CO₂ flux in the
1193 north Indian Ocean. *Ocean Dynamics*, 63(2), 165-178.
- 1194 Valsala, V., Sreesh, M. G., & Chakraborty, K. (2020). The IOD impacts on the Indian
1195 Ocean Carbon cycle. *Journal of Geophysical Research: Oceans*, 125(11), e2020JC016485.
- 1196 Valsala, V., Sreesh, M. G., Anju, M., Sreenivas, P., Tiwari, Y. K., Chakraborty, K., &
1197 Sijikumar, S. (2021). An observing system simulation experiment for Indian Ocean surface
1198 pCO₂ measurements. *Progress in Oceanography*, 194, 102570.
- 1199 Wanninkhof, R. (1992). Relationship between wind speed and gas exchange over the
1200 ocean. *Journal of Geophysical Research: Oceans*, 97(C5), 7373-7382.
- 1201 Wanninkhof, R. (2014). Relationship between wind speed and gas exchange over the ocean
1202 revisited. *Limnology and Oceanography: Methods*, 12(6), 351-362.
- 1203 Watson, A. J., Schuster, U., Shutler, J. D., Holding, T., Ashton, I. G., Landschützer, P., et al.
1204 (2020). Revised estimates of ocean-atmosphere CO₂ flux are consistent with ocean carbon
1205 inventory. *Nature communications*, 11(1), 1-6.
- 1206 Xie, S. P., Annamalai, H., Schott, F. A., & McCreary Jr, J. P. (2002). Structure and
1207 mechanisms of South Indian Ocean climate variability. *Journal of Climate*, 15(8), 864-878.
- 1208 Yadav, K., Rao, V. D., Sridevi, B., & Sarma, V. V. S. S. (2021). Decadal variations in natural
1209 and anthropogenic aerosol optical depth over the Bay of Bengal: the influence of pollutants
1210 from Indo-Gangetic Plain. *Environmental Science and Pollution Research*, 28(39), 55202-
1211 55219.
- 1212 Ye, H., Sheng, J., Tang, D., Morozov, E., Kalhor, M. A., Wang, S., & Xu, H. (2019).
1213 Examining the Impact of Tropical Cyclones on Air-Sea CO₂ Exchanges in the Bay of Bengal
1214 Based on Satellite Data and In Situ Observations. *Journal of Geophysical Research:*
1215 *Oceans*, 124(1), 555-576.
- 1216 Zhang, J., & Reid, J. S. (2010). A decadal regional and global trend analysis of the aerosol
1217 optical depth using a data-assimilation grade over-water MODIS and Level 2 MISR aerosol
1218 products. *Atmospheric Chemistry and Physics*, 10(22), 10949-10963.
- 1219 Zeng, J., Nojiri, Y., Landschützer, P., Telszewski, M., & Nakaoka, S. I. (2014). A global
1220 surface ocean f CO₂ climatology based on a feed-forward neural network. *Journal of*
1221 *Atmospheric and Oceanic Technology*, 31(8), 1838-1849.

1222 Table 1: Details of the hindcast models (including regional models) with reference to a period of the run, products used, parameterization of
 1223 transfer velocity and resolution of the model.
 1224

Global hindcast model	Period for Analysis	Spun-up	Initial conditions/physical forcing	wind	Riverine input used	Transfer velocity	resolution
CCSM-WHOI	1958-2017						$1^0 \times 1^0$
CESM-ETHZ	1980-2018	Spun-up to preindustrial steady state with 287.4 ppm	POP2 model was initialized with Levitus data and state of rest Does not include the phosphoric and silicic acid systems	JRA	No	Wanninkhof 1992	$\sim 1^0 \times 1.125^0$
CNRM-ESM2-1	1980-2018	Preindustrial; 1850 global average CO2 set to 286.46 ppm	Physical: NCEP-2; air-sea flux data: CORE II; atm.CO2: GCP Global averaged annual CO2 Includes the phosphoric and silicic acid systems		Yes	Wanninkhof 2014	$1^0 \times 1^0$
EC-Earth3	1980-2018	Preindustrial steady state 284.32 ppm for 1850	O2, Nutrients: WOA13 DIC, Alkalinity: GLODAPv2; Freshwater input: OMIP2 from JRA1.4-55	JRA55	Yes	Wanninkhof 1992	1×1^0
FESOM_REcoM_LR (FESOM-1.4-REcoM2-LR)	1981-2019	Physical spun-up on HR mesh 1 with constant atm. CO2 BGC fields on LR mesh of 1980 year 278 ppm	atm.CO2: GCP Global averaged annual CO2 O2, Nutrients: WOA13 DIC, Alkalinity: GLODAPv2	JRA55	No	Wanninkhof 2014	$1^0 \times 1^0$
MOM6-Princeton	1980-2018	Atm. CO2 for preindustrial steady state: 278 ppm, Spun-up starting from 1959,	SST, SSS, nutrients: WOA13; DIC & Alkalinity: GLODAPv2; does not include Phosphoric and silicic acid systems. Alkalinity is influenced by inputs from river, calcium carbonate burial to the sediment and nitrogen redox change	JRA	Yes	Wanninkhof 1992	$0.5^0 \times 0.5^0$
MPIOM-HAMOCC	1980-2019	Preindustrial steady state 296.2 ppm atm.CO2	Atmospheric CO2 concentrations are according to the link provided in the RECCAP2 protocol Included phosphoric and silicic acid systems	NCEP	No	Wanninkhof 1992 & 2014	Bipolar grid with 1.5^0 near equator
MRI-ESM2-1	1980-2018	Preindustrial steady state 284.32 ppm	Initialized with those derived from GLODAPv2 and WOA13v2. SST, SSS, nutrients: WOA13v2	JRA 55	No	Wanninkhof 1992 & 2014	Nominally 100 km
NorESM-OC1.2	1980-2018	Preindustrial steady state	Nutrients: WOA13;		No	Wanninkhof 1992	Nominal 1^0

		for 1000 years CO2 set to 278 ppm	DIC and Alkalinity: GLODAPv2 Included phosphoric and silicic acid systems				
ORCA1_LIM3-PISCES (IPSL-NEMO-PISCES)	1980-2018	Initialized with observations in year 1836 and CO2 set to 286.46 ppm at 1870 level	DIC & Alkalinity GLODAPv2 Included phosphoric and silicic acid systems	JRA55	Yes	Wanninkhof 1992	1 ⁰ x 1 ⁰
ORCA025-GEOMAR	1980-2018	Preindustrial steady state for 137 years and CO2 set to 284.32 ppm	Levitus 1998; (SST & SSS) Nutrients: WOAv2 DIC & Alk: GLODAP Pre-spin-up for sea ice from different experiments	JRA55	No	Wanninkhof 1992	1/4 ⁰
Planktom12	1980-2018	Spun-up to 1750-1947 with looped 1990 NCEP forcing; Preindustrial steady state 278 ppm	NCEP forcing Sea-ice: NEMO-LIM2 model Included phosphoric and silicic acid systems			Wanninkhof 1992	1 ⁰ x 1 ⁰
Regional hindcast models							
INCOIS-BIO-ROMS	1980-2018	Initialized with observations for a particular year (1970) RECCAP2 Strategy 1	Atm.CO2: Keeling et.al., 1995 at monthly resolution. The physical state variables have been initialized using ECDA system simulated reanalysis data produced by GFDL. The biological state variables (NO3, Chlorophyll-a, O2, etc.) have been initialized using the climatological state of January generated from the climatological run of the model. The model state of the carbon state variables has been initialized using the Global Ocean Data Product (GLODAP; Key et al., 2004).	JRA55-do	Yes	Wanninkhof 2014	1/12 ⁰
ROMS-NYUAD	1980-2018	1950-1979 (repeated normal year for physical forcing, increasing pCO2 from Joos and Spahni (2008) and Keeling et al. (2005).	temp, salinity, u, v, SSH: ORAS5; O2 & nitrate: WOA18 Chl-a: CMEMS (SeaWiFS& MODIS) DIC & Alk, GLODAPv2	ERA-Interim	Yes	Wanninkhof 1992	0.1 x 0.1

1226
 1227 Table 2: The methods used in the different observation-based surface CO₂ models used in this study.
 1228
 1229

Observation-based surface CO₂ models	Method	Reference
CMEMS-LSCE-FFNN	Feed Forward Neural Network (FFNN)	Chau et al., 2022
CSIRML6	Machine Learning/CSIR-ML6	Gregor et al., 2019
Jena-MLS (CarboScope)	/ocean mixed layer model	Rodenbeck et al., 2013
JMAMLR	Multiple Linear Regression model	Iida et al., 2021
SpcO ₂ LDEO HPD	Global Ocean Biogeochem Model/Extreme Gradient Boosting (XGB)	Gloege et al., 2022
SOMFNN	Neural Network	Landschutzer et al., 2016
NIES-MLR3	Feed Forward Neural Network (FFNN)	Zeng et al., 2014
OceanSODAETHZ	Geospatial Random Cluster Ensemble Regression (GRaCER)	Gregor and Gruber 2021
UOEX WAT20	Multiple Linear Regression/ Feed Forward Neural Network (FFNN)	Watson et al., 2020

1230
 1231

1232 Table 3: The annual mean uptake (\pm standard deviation) of CO₂ from the climatology (Takahashi et al, 2009), hindcast, empirical and atmospheric
 1233 inversion models. All units in PgC yr⁻¹. The negative values represent CO₂ flux into the ocean and the positive ones into the atmosphere.
 1234
 1235

Region	Climatology	Hindcast Models (Includes 2 Regional models) (n=14)	Observation- based models (n=9)	Atmospheric Inversion models (n=2)	All models (n=25)	Surface area (km ²)
Arabian Sea	0.08 \pm 0.06	0.03 \pm 0.01	0.08 \pm 0.01	0.16 \pm 0.12	0.06 \pm 0.05	0.70 x 10 ⁷
Bay of Bengal	0.01 \pm 0.01	-0.00 \pm 0.01	0.01 \pm 0.00	0.01 \pm 0.01	0.00 \pm 0.01	0.44 x 10 ⁷
Equatorial Indian Ocean	0.04 \pm 0.03	-0.05 \pm 0.04	0.02 \pm 0.02	0.02 \pm 0.03	-0.02 \pm 0.05	1.55 x 10 ⁷
South Indian Ocean	-0.20 \pm 0.16	-0.19 \pm 0.06	-0.23 \pm 0.02	-0.46 \pm 0.30	-0.23 \pm 0.11	1.24 x 10 ⁷
Indian Ocean	-0.07 \pm 0.14	-0.21 \pm 0.10	-0.13 \pm 0.04	-0.27 \pm 0.16	-0.19 \pm 0.10	3.92 x 10 ⁷

1236
 1237
 1238
 1239
 1240
 1241
 1242
 1243
 1244
 1245
 1246
 1247
 1248
 1249
 1250
 1251

1252 Table 4: The growth rate (\pm standard deviation) of pCO₂ (μ atm yr⁻¹) in the different regions of the Indian Ocean and different periods. The p-
 1253 value of the regression of time-series pCO₂ variability is given in bracket.
 1254

Period (μ atm/yr)	Arabian Sea		Bay of Bengal		Equatorial Indian Ocean		South Indian Ocean		Indian Ocean	
	hindcast	Empirical	hindcast	Empirical	hindcast	Empirical	hindcast	Empirical	hindcast	Empirical
1985-2018	1.68 \pm 0.03 (7.7E-32)	1.64 \pm 0.02 (1.8E-39)	1.54 \pm 0.04 (5.4E-28)	1.64 \pm 0.02 (7.2E-38)	1.72 \pm 0.03 (1.1E-31)	1.65 \pm 0.02 (1.3E-38)	1.73 \pm 0.03 (1.8E-32)	1.70 \pm 0.02 (2.6E-37)	1.70 \pm 0.03 (4.6E-33)	1.67 \pm 0.02 (4.7E-39)
1985-2000	1.32 \pm 0.07 (3.7E-11)	1.41 \pm 0.04 (3.3E-15)	1.34 \pm 0.15 (5.2E-07)	1.46 \pm 0.05 (1.4E-13)	1.43 \pm 0.09 (1.6E-10)	1.52 \pm 0.04 (5.00E-15)	1.43 \pm 0.08 (6.9E-11)	1.50 \pm 0.05 (4.6E-14)	1.41 \pm 0.08 (2.9E-11)	1.49 \pm 0.04 (1.6E-15)
2001-2018	1.88 \pm 0.06 (2.1E-15)	1.76 \pm 0.03 (9.6E-21)	1.71 \pm 0.06 (1.6E-14)	1.76 \pm 0.05 (4.7E-17)	2.01 \pm 0.05 (5.2E-17)	1.82 \pm 0.04 (1.30E-17)	1.98 \pm 0.05 (9.4E-17)	1.91 \pm 0.03 (8.1E-21)	1.96 \pm 0.04 (3.9E-18)	1.84 \pm 0.03 (9.3E-20)

1255
 1256
 1257
 1258
 1259
 1260
 1261
 1262
 1263
 1264

1265 Table 5: Rate of changes in CO₂ fluxes (\pm standard deviation) (PgC yr⁻¹ decade⁻¹) in the Indian Ocean during different time periods. The p-value
 1266 of the regression of time-series CO₂ variability is given in bracket. The negative values represent the decrease in source and vice versa for the
 1267 positive.
 1268
 1269

Period	Arabian Sea		Bay of Bengal		Equatorial Indian Ocean		South Indian Ocean		Indian Ocean	
	hindcast	Empirical	hindcast	Empirical	hindcast	Empirical	hindcast	Empirical	hindcast	Empirical
1985-2018	-0.003 \pm 0.001 (3.5E-05)	-0.006 \pm 0.001 (2.7E-09)	-0.004 \pm 0.000 (2.4E-09)	-0.002 \pm 0.0001 (3.14E-05)	-0.007 \pm 0.001 (7.3E-06)	-0.006 \pm 0.002 (6.0E-04)	-0.010 \pm 0.002 (1.9E-05)	-0.008 \pm 0.002 (1.8E-05)	-0.023 \pm 0.003 (1.4E-08)	-0.021 \pm 0.003 (1.2E-07)
1985-2000	-0.001 \pm 0.002 (5.4E-01)	-0.002 \pm 0.002 (4.7E-01)	-0.002 \pm 0.002 (2.4E-01)	0.001 \pm 0.001 (2.3E-01)	-0.004 \pm 0.005 (3.7E-01)	0.010 \pm 0.003 (4.2E-03)	-0.020 \pm 0.006 (4.2E-03)	-0.003 \pm 0.005 (5.0E-01)	-0.028 \pm 0.012 (3.2E-02)	0.007 \pm 0.007 (3.7E-01)
2001-2018	-0.005 \pm 0.002 (7.8E-03)	-0.011 \pm 0.001 (1.8E-07)	-0.005 \pm 0.001 (3.0E-06)	-0.005 \pm 0.0001 (8.5E-09)	-0.006 \pm 0.003 (8.1E-02)	-0.018 \pm 0.002 (1.1E-07)	-0.006 \pm 0.005 (2.0E-01)	-0.012 \pm 0.004 (9.1E-03)	-0.023 \pm 0.007 (4.0E-03)	-0.046 \pm 0.005 (6.2E-08)

1270 Figure 1: a) Figure showing the sub-regions of the Indian Ocean used in this study: South
1271 Indian Ocean (SIO; Brown), equatorial Indian Ocean (EIO; red), Arabian Sea (AS; Blue) and
1272 Bay of Bengal (BoB; green). b) shows the location of observations of oceanic pCO₂ collected
1273 since 1958 (Bakker et al., 2020), c) CO₂ flux climatology based on the observations and
1274 interpolated to a 4 x 5° grid (Takahashi et al., 2009) and d) Annual mean uptake from
1275 climatology, hindcast, empirical and atmospheric inversions models (PgC yr⁻¹) for the
1276 reference year of 2002. The error bars represent the standard deviation. The negative values
1277 represent fluxes into the ocean and positive to the atmosphere.

1278
1279 Figure 2: Annual mean uptake (in mol m⁻² yr⁻¹) from the 14 hindcasts (2 regional) models for
1280 the reference year of 2002. The negative values reflect fluxes into the ocean and are positive
1281 for the atmosphere.

1282
1283 Figure 3: Annual mean uptake (in mol m⁻² yr⁻¹) from the 9 observation-based models for the
1284 reference year of 2002. The negative values reflect fluxes into the ocean and are positive for
1285 the atmosphere.

1286
1287 Figure 4: Annual mean uptake (in mol m⁻² yr⁻¹) from the 2 atmospheric inversion models. The
1288 CAMSv20r1 used inter-annually varying prior fluxes from an empirical model CEMES,
1289 while MACTM used annually repeating prior flux seasonality from Takahashi et al. (2009).
1290 The negative values reflect fluxes into the ocean and are positive for the atmosphere.

1291
1292 Figure 5: The zonally integrated, annual mean CO₂ uptake (30°N-37.5°S) from a) hindcast, b)
1293 empirical and c) atmospheric inversion models.

1294
1295 Figure 6: Seasonal cycle of the CO₂ fluxes (PgC yr⁻¹; left panel) and δpCO₂ (µatm; right
1296 panel) in the Indian Ocean from observations, mean hindcast, empirical and atmospheric
1297 inversion models in the Indian Ocean, Arabian Sea, BoB, EIO and SIO.

1298
1299 Figure 7: The inter-annual variability from hindcast, empirical and atmospheric inversion
1300 models. The upper panel shows the ENSO (<https://ggweather.com/enso/oni.htm>) and IOD
1301 index (<http://www.bom.gov.au/climate/iod/>) and the other panels for the entire Indian Ocean,
1302 Arabian Sea, Bay of Bengal, equatorial Indian Ocean, and South Indian Ocean. The trends of
1303 mean hindcast, empirical and atmospheric inversion are given in PgC yr⁻¹ decade⁻¹.

Figure 1.

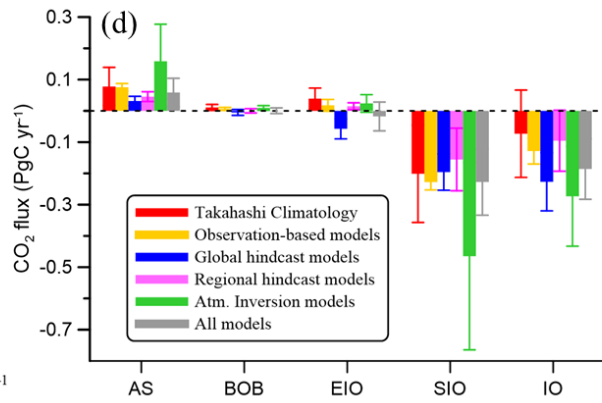
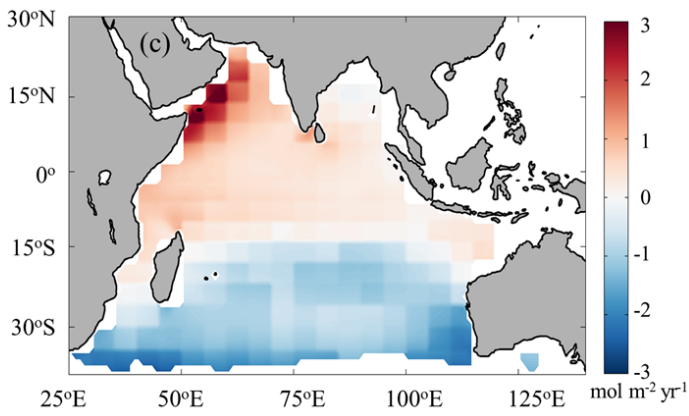
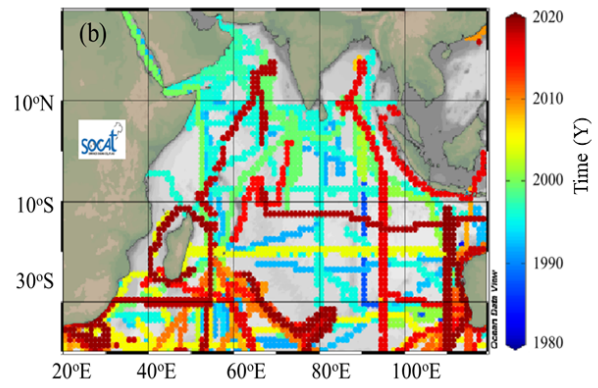
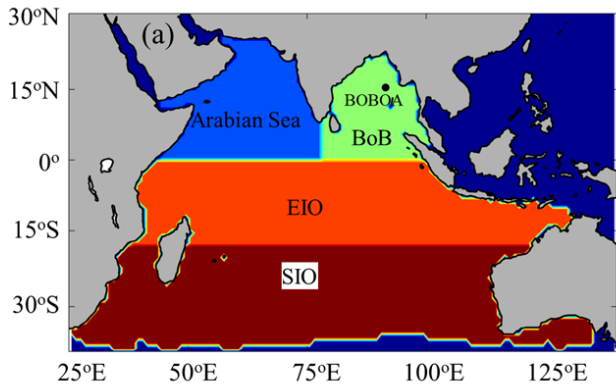


Figure 2.

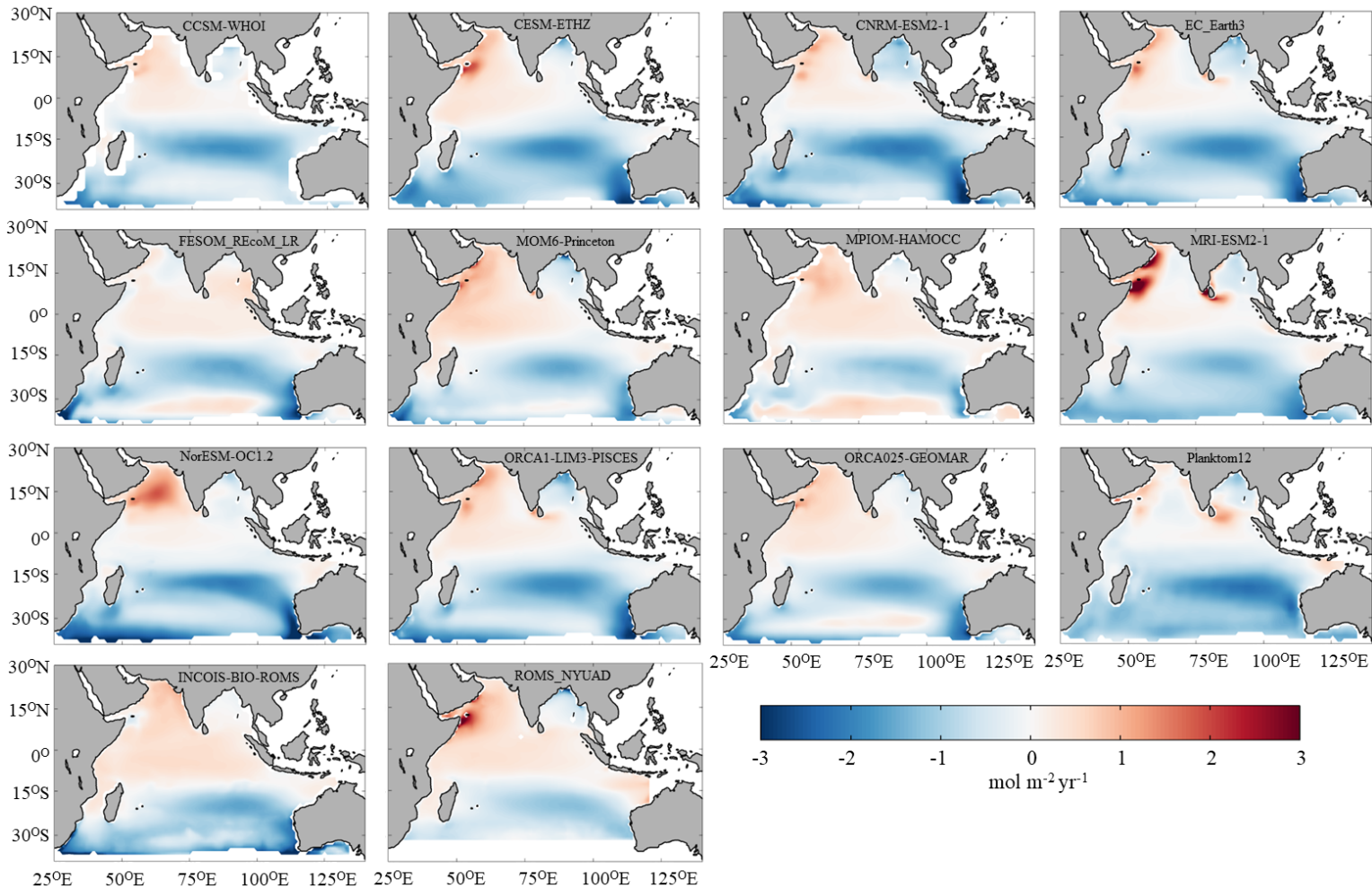


Figure 3.

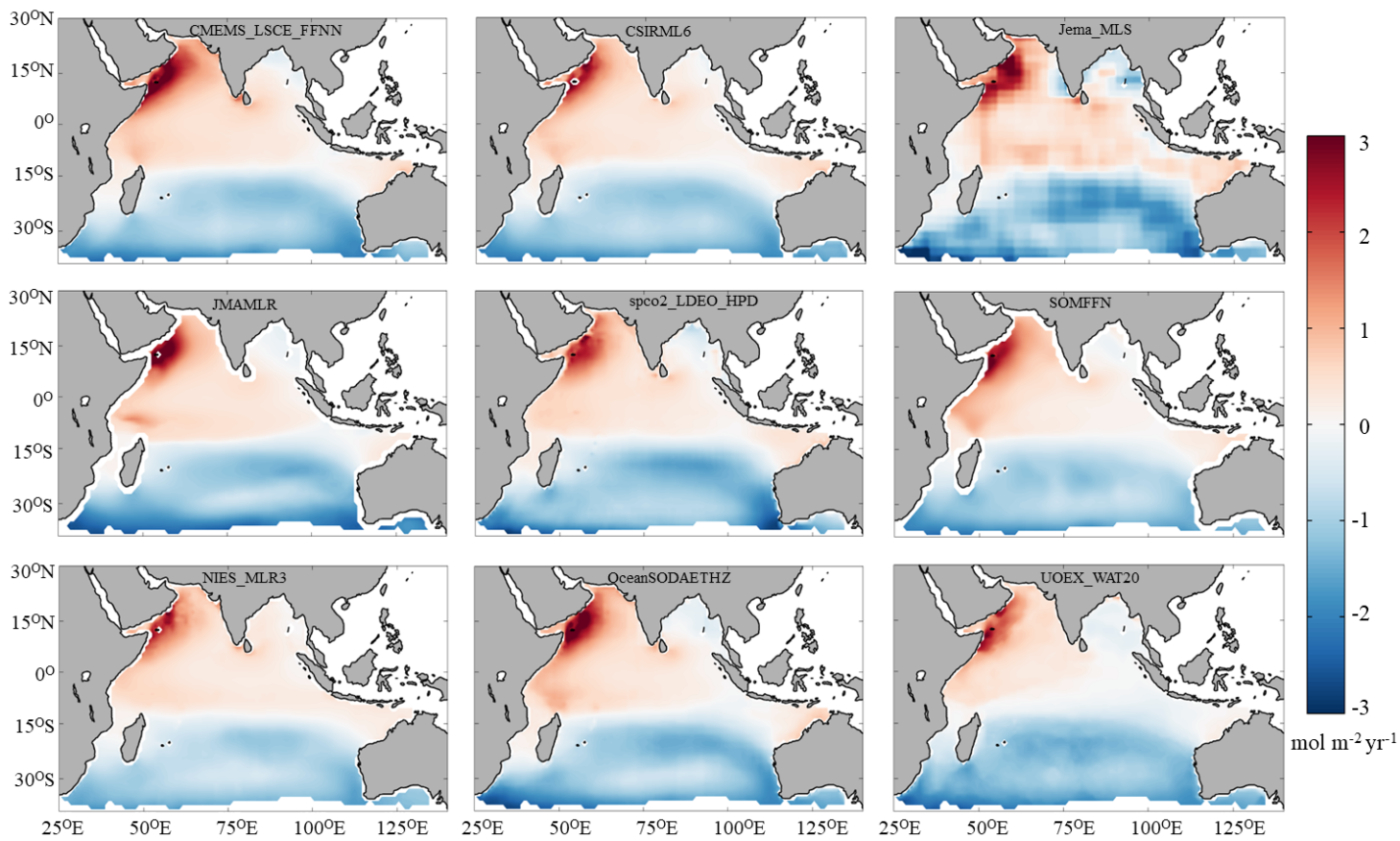


Figure 4.

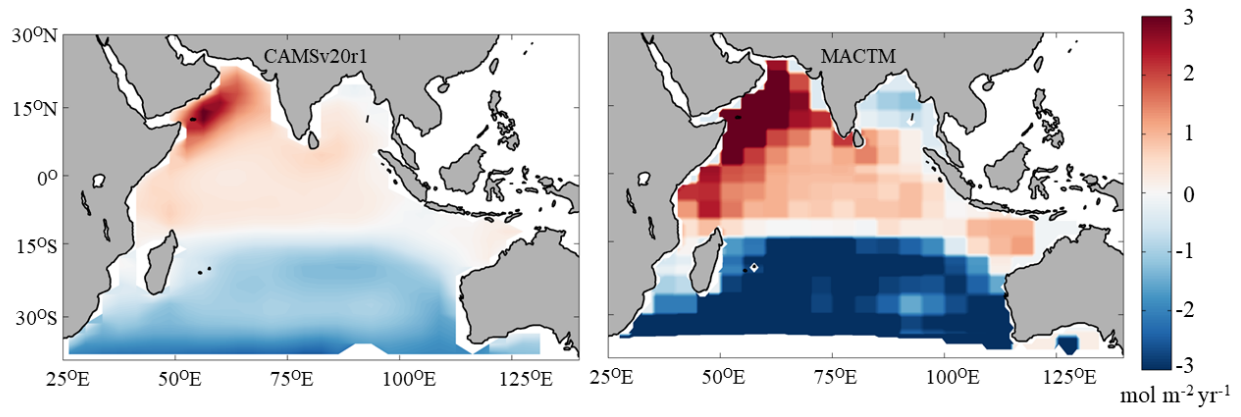


Figure 5.

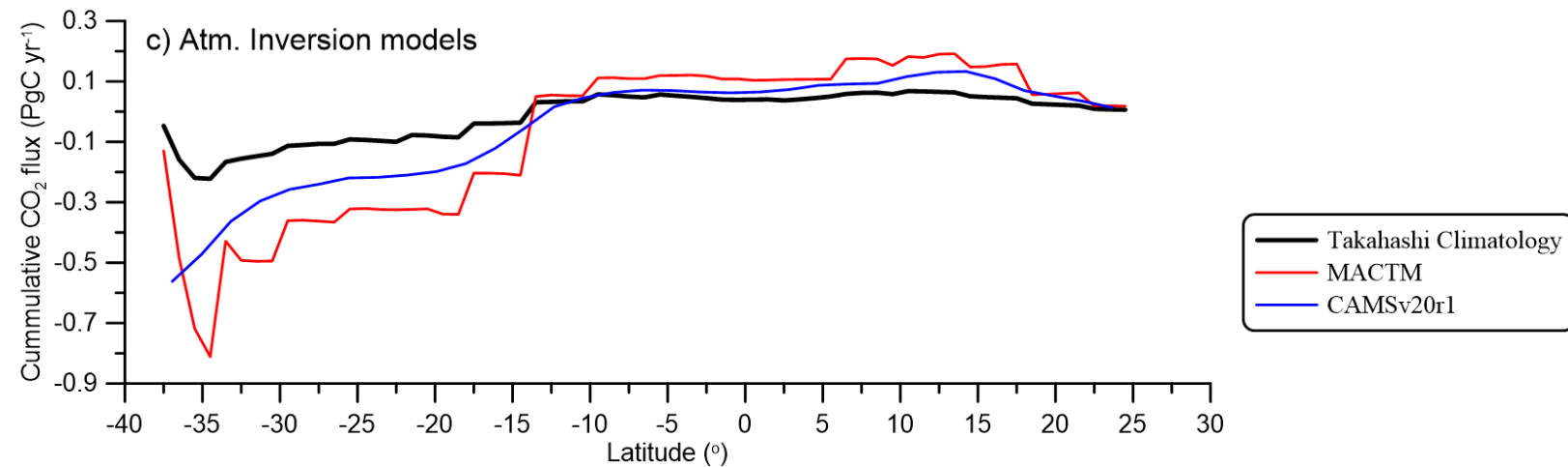
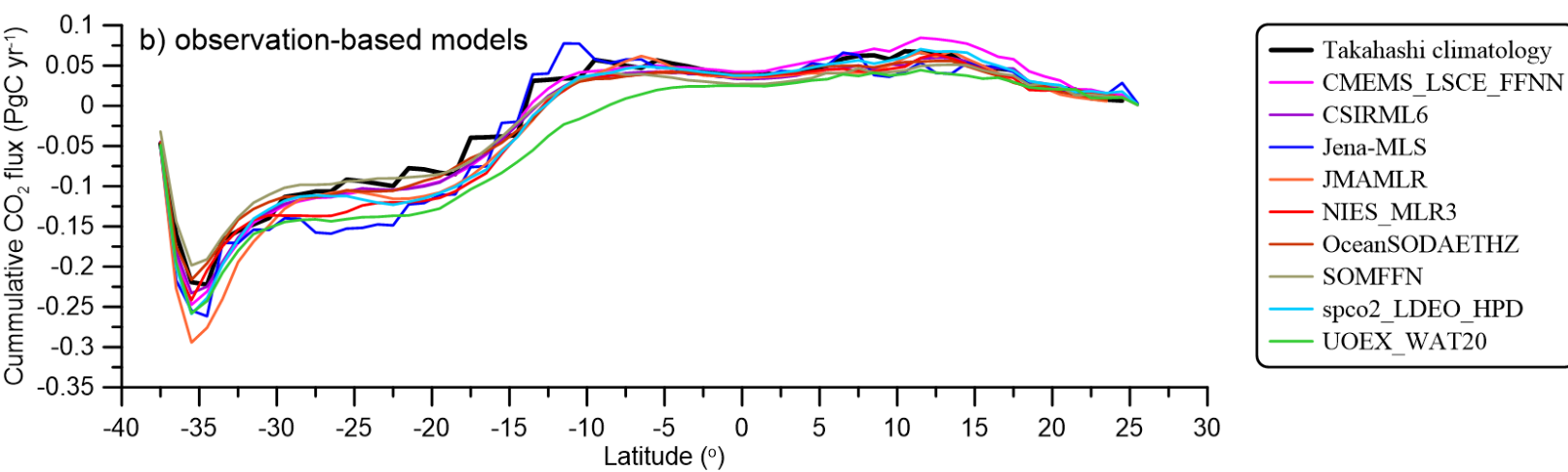
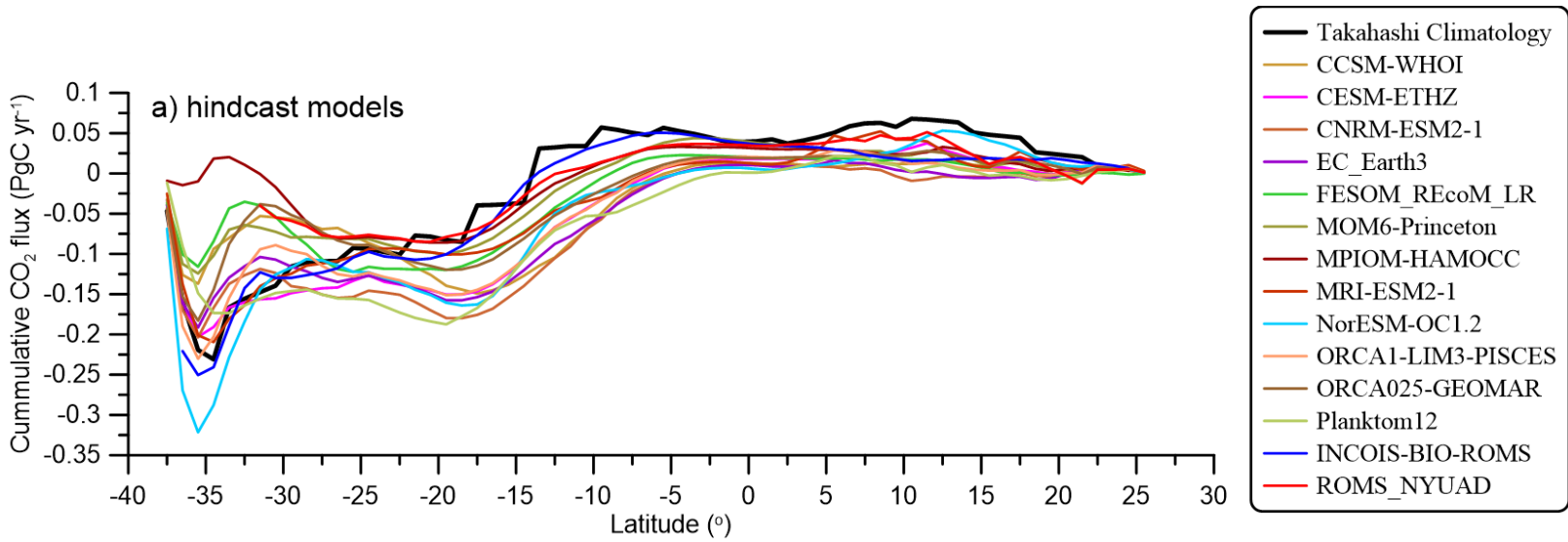


Figure 6.

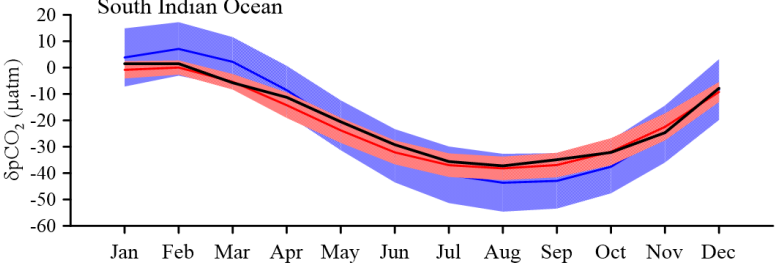
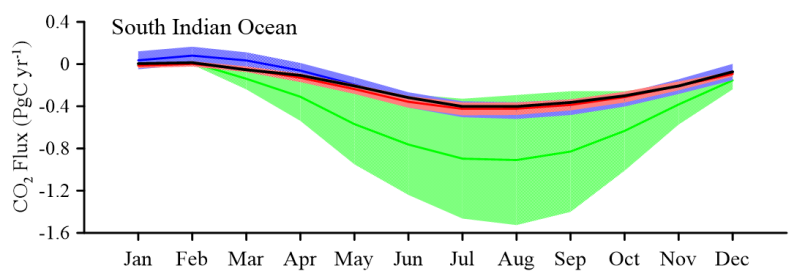
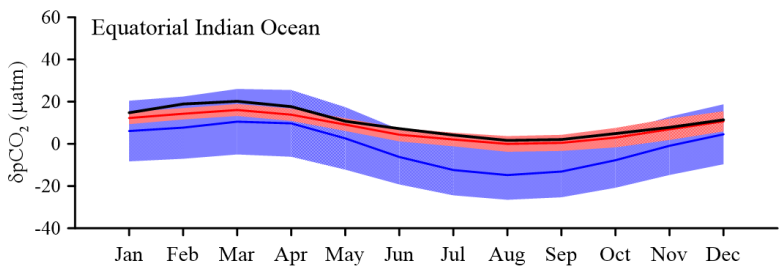
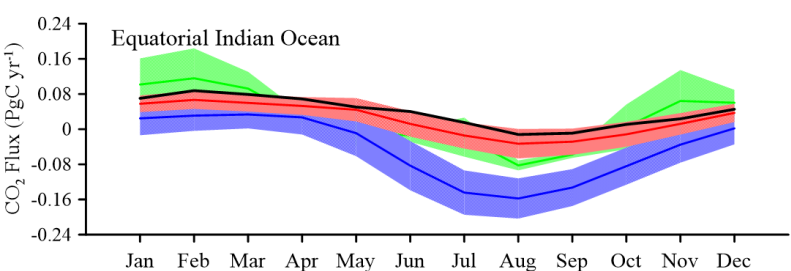
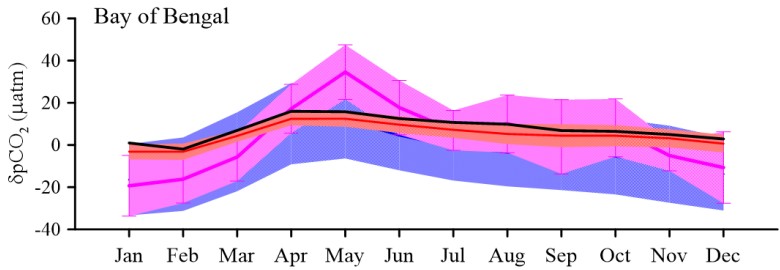
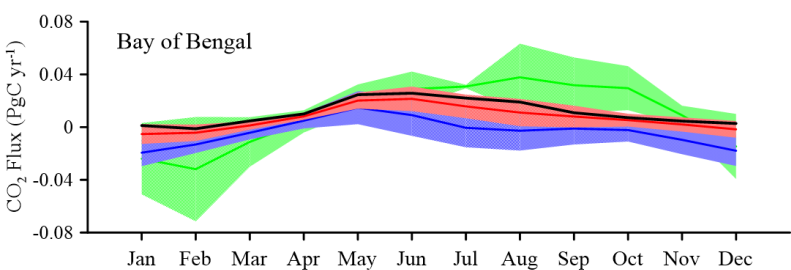
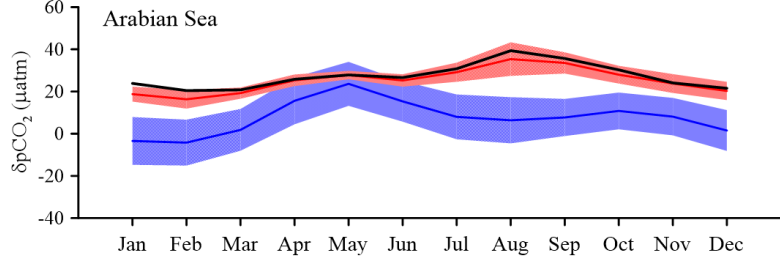
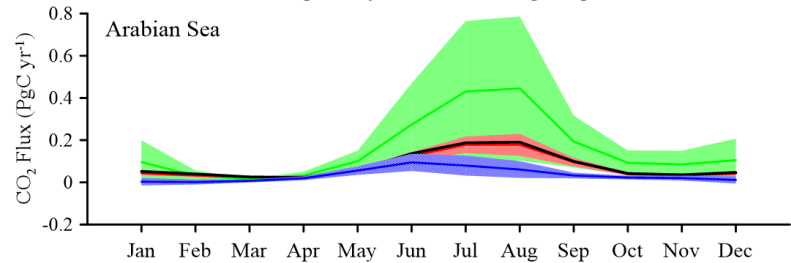
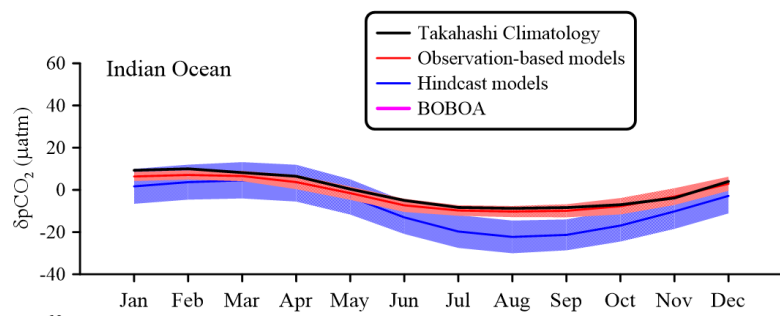
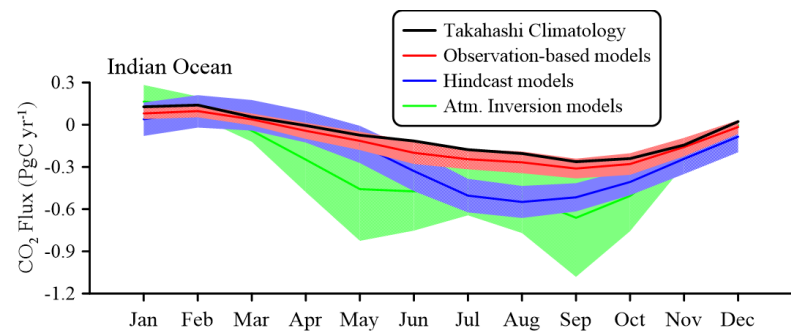


Figure 7.

